

Signature of Metallic Behavior in the Metal–Organic Frameworks $M_3(\text{hexaminobenzene})_2$ ($M = \text{Ni}, \text{Cu}$)

Jin-Hu Dou,[†] Lei Sun,[†] Yicong Ge,[†] Wenbin Li,[‡] Christopher H. Hendon,[†] Ju Li,[§] Sheraz Gul,[⊥] Junko Yano,[⊥] Eric A. Stach,[#] and Mircea Dincă^{*,†}

[†]Department of Chemistry, Massachusetts Institute of Technology, 77 Massachusetts Avenue, Cambridge, Massachusetts 02139, United States

[‡]Research Laboratory of Electronics, Massachusetts Institute of Technology, 77 Massachusetts Avenue, Cambridge, Massachusetts 02139, United States

[§]Department of Nuclear Science and Engineering, Department of Materials Science and Engineering, Massachusetts Institute of Technology, 77 Massachusetts Avenue, Cambridge, Massachusetts 02139, United States

[⊥]Molecular Biophysics and Integrated Bioimaging Division, Lawrence Berkeley National Laboratory, Berkeley, California 94720, United States

[#]Center for Functional Nanomaterials, Brookhaven National Laboratory, Upton, New York 11973, United States

Supporting Information

ABSTRACT: The two-dimensionally connected metal–organic frameworks (MOFs) $\text{Ni}_3(\text{HIB})_2$ and $\text{Cu}_3(\text{HIB})_2$ (HIB = hexaminobenzene) are bulk electrical conductors and exhibit ultraviolet-photoelectron spectroscopy (UPS) signatures expected of metallic solids. Electronic band structure calculations confirm that in both materials the Fermi energy lies in a partially filled delocalized band. Together with additional structural characterization and microscopy data, these results represent the first report of metallic behavior and permanent porosity coexisting within a metal–organic framework.

Recent progress in the synthesis of electrically conductive metal–organic frameworks (MOFs) has enabled applications that were previously thought impractical for this traditionally insulating set of materials.¹ Examples include the use of neat MOFs as active electrodes in electrocatalysis,^{2,3} batteries,^{4,5} chemiresistive sensors,^{6,7} thermoelectric devices,⁸ supercapacitors,⁹ electrochromic devices,¹⁰ and field effect transistors (FETs).¹¹ Many of these applications are served better by semiconducting MOFs, others would see considerable improvements if the MOFs were metallic. However, there are thus far no examples of metallic MOFs, and demonstrating metallic behavior remains an important challenge of fundamental interest. Along this line, the only materials in this class that exhibit a bulk conductivity greater than 10 S/m at room temperature are $\text{Ni}_3(2,3,6,7,10,11\text{-hexaminotriphenylene})_2$ ($\text{Ni}_3(\text{HITP})_2$),¹² $\text{Ni}_3(\text{benzenehexathiol})_2$ ($\text{Ni}_3(\text{BHT})_2$),¹³ and $\text{Cu}_3(\text{benzenehexathiol})_2$ ($\text{Cu}_3(\text{BHT})_2$).¹⁴ All three belong to a subclass of hexagonal layered structures wherein trigonal organic ligands and square-planar mononuclear metal nodes define two-dimensional (2D) sheets whose electronic structure enables excellent electron delocalization through continuous conjugation.

Relevantly, theoretical studies of these 2D materials predicted that some should behave as bulk metals,^{13,15–17} yet experimental

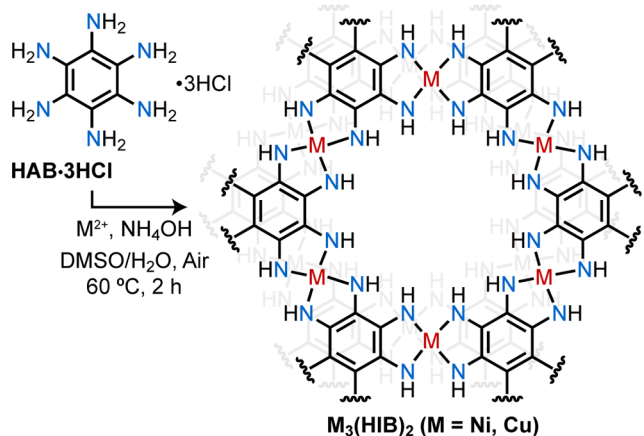
evidence for metallic behavior in these remains elusive.¹³ We surmised that replacing 2,3,6,7,10,11-hexaminothriphenylene (HITP) by the smaller hexaminobenzene (HIB) would reduce the distance and provide better overlap between the electronic wave functions of neighboring metals/ligands in $\text{Ni}_3(\text{hexaminobenzene})_2$ ($\text{Ni}_3(\text{HIB})_2$), leading possibly to metallicity. However, recently reported FETs made from films of $M_3(\text{HIB})_2$ ($M = \text{Ni}, \text{Co}, \text{Cu}$) exhibited responses characteristic of insulators or materials with very low conductance, at best.¹⁸ We contended that this surprisingly insulating behavior was due to the severe disorder and poor crystallinity of the films, as evidenced also by selected area electron diffraction (SAED), and that more crystalline samples would reveal different information about the intrinsic properties of these materials. Accordingly, on the premise that HIB-based frameworks continue to be ideal candidates for metallic MOFs, we set out to devise new synthetic pathways for accessing high quality and crystalline samples of these materials and explore their electrical properties.

Here, we show that crystalline $\text{Ni}_3(\text{HIB})_2$ and $\text{Cu}_3(\text{HIB})_2$, characterized by X-ray diffraction, spectroscopic analysis, and high resolution transmission electron microscopy (HRTEM), are indeed excellent conductors, with pellet conductivities averaging approximately 1000 S/m at 300 K and under vacuum (Scheme 1). Significantly, ultraviolet-photoelectron spectroscopy (UPS) and electronic band structure calculations evidence intrinsic metallic behavior in both materials.

Black microcrystalline samples of $M_3(\text{HIB})_2$ ($M = \text{Ni}, \text{Cu}$) were isolated from reactions of hexaaminobenzene trihydrochloride ($\text{HAB}\cdot 3\text{HCl}$) with ammoniacal solutions of $\text{Ni}(\text{NO}_3)_2\cdot 6\text{H}_2\text{O}$ or $\text{CuSO}_4\cdot 5\text{H}_2\text{O}$ in mixtures of water and dimethyl sulfoxide heated at 60 °C in air for 2 h. The presence of O_2 is essential for the isolation of crystalline materials; the absence of air yields only amorphous gray powders. Scanning electron microscopy (SEM) showed that the products consist of

Received: July 11, 2017

Published: September 14, 2017

Scheme 1. Synthesis of $\text{Ni}_3(\text{HIB})_2$ and $\text{Cu}_3(\text{HIB})_2$ 

irregularly shaped nanoparticles smaller than 100 nm (Figure S3). Inspection of the $\text{M}(2p)$ and $\text{N}(1s)$ regions of the high resolution X-ray photoelectron spectra (XPS, Figures S4 and S5) evidenced chemical environments consistent with square planar metal ions and anilinic N atoms in both materials. Additional extra-framework M^{2+} or NH_4^+ ions, the only possible charge-balancing cations for a potentially negatively charged MOF would appear at different regions in the XPS; their absence confirms the neutral state of $\text{M}_3(\text{HIB})_2$.

Thermogravimetric analysis (TGA) revealed that both $\text{Ni}_3(\text{HIB})_2$ and $\text{Cu}_3(\text{HIB})_2$ desolvate above 100 °C and likely decompose above 200 °C, as evidenced by the more pronounced weight losses above this temperature (Figure S6). Evacuation at 120 °C under dynamic vacuum for 24 h followed by N_2 sorption analysis revealed type II isotherms with uptakes of 82 and 65 cm^3/g at 77 K and apparent Brunauer–Emmett–Teller (BET) surface areas of 152 and 114 m^2/g for $\text{Ni}_3(\text{HIB})_2$ and $\text{Cu}_3(\text{HIB})_2$, respectively (Figure S7). These values are in line with those of other 2D materials exhibiting similar pore size (vide infra).

Synchrotron powder X-ray diffraction (PXRD) confirmed a high degree of crystallinity: both materials exhibit prominent diffraction peaks at $2\theta = 2.54^\circ, 5.18^\circ, 6.81^\circ, 8.10^\circ, 9.07^\circ, 14.27^\circ,$ and 18.97° (Figures 1, S8, and S9). Indexing of these peaks revealed hexagonal unit cells with lattice parameters $a = 13.5(2)$ Å and $c = 3.3(1)$ Å. To determine the precise interlayer stacking sequence, we performed Ni and Cu K-edge extended X-ray absorption fine structure (EXAFS) analysis. $\text{Ni}\cdots\text{Ni}$ and $\text{Cu}\cdots\text{Cu}$ scattering paths at $R = 3.60 \pm 0.09$ Å and $R = 3.33 \pm 0.10$ Å were required to fit the EXAFS spectra of $\text{Ni}_3(\text{HIB})_2$ and $\text{Cu}_3(\text{HIB})_2$, respectively (Figure S10). Both $\text{M}\cdots\text{M}$ distances determined by EXAFS analysis exceed the interlayer distance observed by PXRD, suggesting that the 2D layers are not perfectly eclipsed and that significant (ab) shifting occurs in both materials between neighboring layers. Taken together, the PXRD and EXAFS data give structural models where neighboring layers are shifted by approximately one-quarter cell along one edge of the hexagonal unit cell, thereby lowering the symmetry to orthorhombic. Indeed, Le Bail fitting of the PXRD patterns of the two materials gave best fits for space groups $Cmcm$ and $C222_1$ for $\text{Ni}_3(\text{HIB})_2$ and $\text{Cu}_3(\text{HIB})_2$, respectively (Figure S11), with otherwise identical unit cell parameters $a = 13.5(2)$ Å, $b = 23.3(5)$ Å, and $c = 6.6(1)$ Å.

To understand the difference in symmetry between the Ni and Cu materials, we computed optimized geometries for

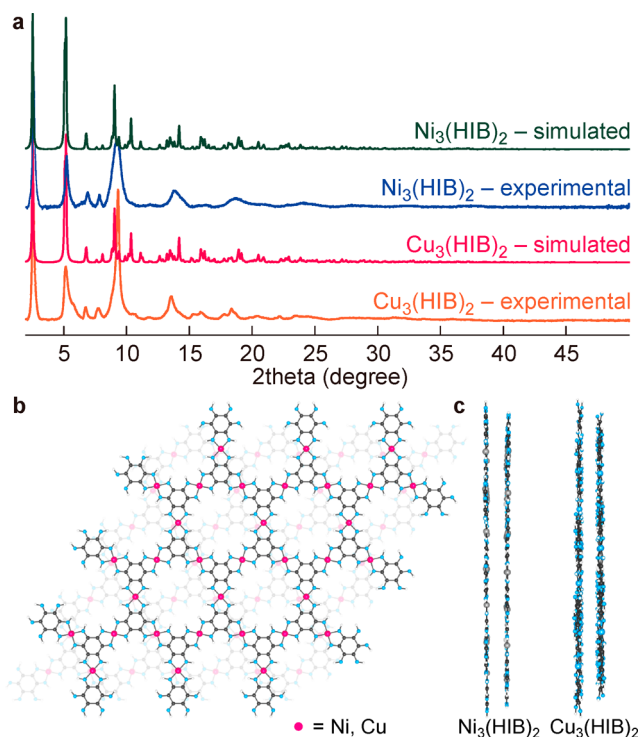


Figure 1. (a) Powder X-ray diffraction patterns. (b,c) Calculated structures of $\text{M}_3(\text{HIB})_2$.

individual 2D sheets using density functional theory (DFT) (Figure S12). This revealed hexagonal lattice constants of 13.48 Å, in agreement with the experimental values. It also revealed that the local symmetry of the Ni^{2+} ions is strictly D_{4h} giving rise to completely planar $\text{Ni}_3(\text{HIB})_2$ monolayers, whereas CuN_4 units distort out-of-plane and give rise to overall buckled 2D layers in $\text{Cu}_3(\text{HIB})_2$ (Figures 1c and S12). We therefore attribute the lack of mirror symmetry in $\text{Cu}_3(\text{HIB})_2$ to the local coordination environment of the Cu^{2+} ions (Figures 1c and S12).

HRTEM provided further evidence of two-dimensional long-range order in $\text{M}_3(\text{HIB})_2$. Most notably, fast Fourier transform (FFT) analysis of the images in Figure 2 revealed honeycomb lattices with a lattice parameter $a = 13.5$ Å, in excellent agreement with the values obtained from PXRD analysis and DFT computations. Intriguingly, our microscopy and structural data contrasts with that previously reported for these materials.¹⁸ In particular, it suggests a higher degree of

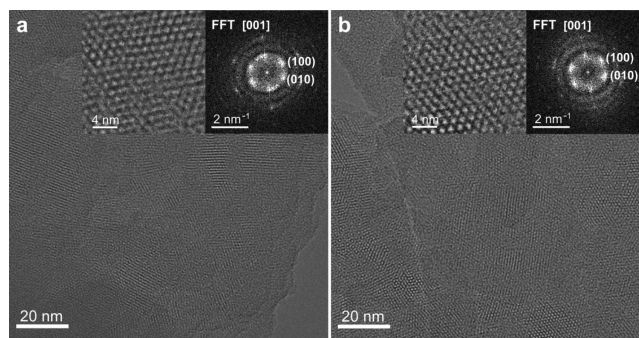


Figure 2. HRTEM image of (a) $\text{Ni}_3(\text{HIB})_2$ and (b) $\text{Cu}_3(\text{HIB})_2$ taken at 300 kV. Insets are high magnification HRTEM images (left) and the corresponding FFT analysis (right).

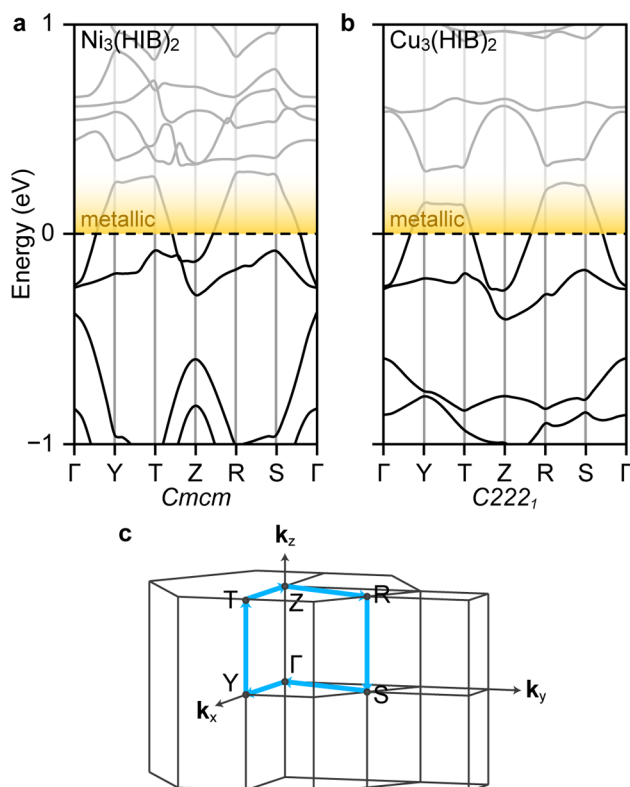


Figure 3. (a,b) Calculated electronic band structure of bulk $\text{Ni}_3(\text{HIB})_2$ and $\text{Cu}_3(\text{HIB})_2$, respectively. (c) Corresponding first Brillouin zone and high-symmetry K-points.

crystallinity and potentially a different structure for our materials, which encouraged us to investigate the electronic properties of $\text{M}_3(\text{HIB})_2$ samples as synthesized here.

Importantly, DFT electronic band structure calculations suggested that both monolayer and bulk $\text{M}_3(\text{HIB})_2$ should be metallic. Monolayers of both Ni and Cu MOFs exhibit electronic band structures featuring two wide bands forming a Dirac cone at the K point, reminiscent of the classic Kagome bands (Figure S13).¹⁹ The Dirac bands cross the Fermi level in both Γ -K and Γ -M directions and have wide band dispersions of approximately 0.8 eV. The projected density of states exhibits considerable contributions from the metal, C, and N orbitals at the Fermi level, confirming the high degree of in-plane π -conjugation expected for these materials.

The electronic band structures of bulk orthorhombic $\text{M}_3(\text{HIB})_2$ plotted along the high symmetry points in the first Brillouin zone are shown in Figure 3 and Figure S14. Salient features include bands crossing the Fermi level in the in-plane Γ -Y, T-Z, Z-R, and Γ -S directions in both materials, which indicates the metallic character of both solids. Notably, because no bands cross the Fermi level in the out-of-plane directions (Y-T and R-S), the bulk materials are expected to be metallic only in the *ab* directions and semiconducting in the *c* direction.

The bulk electrical properties of $\text{M}_3(\text{HIB})_2$ were determined from pelletized samples of the two materials, obtained by pressing powders at approximately 1 GPa. Upon degassing under dynamic vacuum ($\sim 1 \times 10^{-5}$ Torr) at 150 °C, the pellets were imaged with SEM, which revealed small particles with prominent grain boundaries and voids (Figure S15). The electrical conductivity of the pellets, measured by the van der Pauw method (Figure S16) under vacuum and in the dark²⁰ was 800 S/m for $\text{Ni}_3(\text{HIB})_2$ and 1300 S/m in $\text{Cu}_3(\text{HIB})_2$ at 300 K.

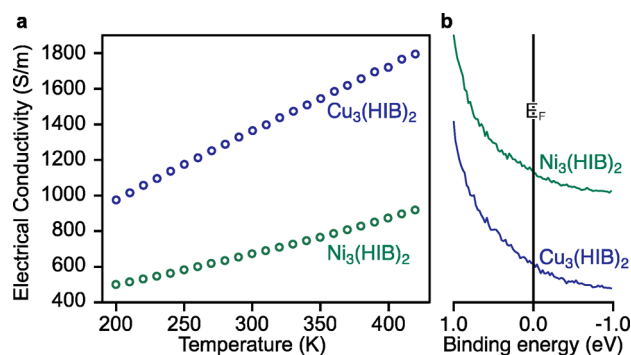


Figure 4. (a) Variable-temperature electrical conductivity of pressed pellets of $\text{M}_3(\text{HIB})_2$ measured by the van der Pauw method under vacuum. (b) UPS of $\text{M}_3(\text{HIB})_2$ acquired at 300 K.

These are among the highest values observed for MOFs, and compare favorably even with the more relevant subset of electrically conducting 2D MOFs.¹

Although a signature of bulk metallic behavior is thermally deactivated transport,²¹ temperature-dependence conductivity measurements revealed that electrical transport in both $\text{Ni}_3(\text{HIB})_2$ and $\text{Cu}_3(\text{HIB})_2$ correlates positively with temperature. Indeed, the electrical conductivity in polycrystalline pellets of both MOFs increases linearly as the temperature increases from 200 to 420 K (Figure 4a). PXRD confirmed that no structural transitions occur in this temperature range (Figure S17). We attribute the observed thermally activated transport, more characteristic of semiconducting rather than metallic behavior, to interparticle rather than intraparticle (i.e., intrinsic) transport. In other words, thermally activated hopping over grain boundaries (i.e., interparticle transport) dominates the temperature dependence of conductivity in the bulk polycrystalline pellets, giving rise to apparent semiconducting behavior in otherwise intrinsically metallic solids. This behavior is indeed well documented for granular metals where inter-grain charge hopping mediates charge transport (Figure S18).²² Further complicating the interpretation of the bulk conductivity of $\text{M}_3(\text{HIB})_2$ is the bimodal transport expected from DFT band structure calculations: metallic in the plane of the MOF sheets, but semiconducting normal to the 2D sheets (vide supra). Because the orientation of particles in the pellets is random, both in-plane and out-of-plane charge transport contribute to bulk conductivity, the latter in line with the observed temperature dependence.

Experimental confirmation of the metallic nature of both MOFs came from UPS, which informs on the intrinsic properties of even polycrystalline samples by measuring the density of states near the Fermi level. Grazing incident wide-angle X-ray scattering (GIWAXS) of $\text{Ni}_3(\text{HIB})_2$ and $\text{Cu}_3(\text{HIB})_2$ films prepared on highly doped silicon (Figure S19), as required for UPS measurements, confirmed the identity of the two MOFs and showed that they preferably orient with a typical face-on packing mode where the 2D sheets are parallel to the silicon substrate (Figure S20).²³ The UPS measurements at 300 K revealed Fermi edges for both $\text{Ni}_3(\text{HIB})_2$ and $\text{Cu}_3(\text{HIB})_2$ (Figures 4b and S21), which are indicative of electronic bands crossing the Fermi level, and are strong evidence for metallic behavior in $\text{M}_3(\text{HIB})_2$.^{13,24}

In conclusion, we show that reaction of hexaaminobenzene with Ni^{2+} or Cu^{2+} under carefully controlled conditions gives rise to porous crystalline materials with bulk electrical

conductivities exceeding 800 S/m. UPS measurements and DFT computational studies evidenced rare metallic behavior in MOFs, a class of notoriously insulating materials. Most importantly, we demonstrate for the first time that metallic behavior and porosity are compatible in these materials. These results encourage further fundamental physical studies and advanced electronic applications, which continue to depend critically on the development of techniques to grow and study single crystals of 2D MOFs, an area of current efforts in our group.

■ ASSOCIATED CONTENT

Supporting Information

The Supporting Information is available free of charge on the ACS Publications website at DOI: 10.1021/jacs.7b07234.

Additional experimental details and characterization data (PDF)

■ AUTHOR INFORMATION

Corresponding Author

*mdinca@mit.edu

ORCID

Jin-Hu Dou: 0000-0002-6920-9051

Lei Sun: 0000-0001-8467-6750

Ju Li: 0000-0002-7841-8058

Junko Yano: 0000-0001-6308-9071

Eric A. Stach: 0000-0002-3366-2153

Mircea Dincă: 0000-0002-1262-1264

Notes

The authors declare no competing financial interest.

■ ACKNOWLEDGMENTS

This work was supported by the Army Research Office (grant number W911NF-17-1-0174). W.L. and J.L. acknowledge support by the Center for Excitons, an Energy Frontier Research Center funded by U.S. Department of Energy, Office of Science, Basic Energy Sciences under Award No. DE-SC0001088. We thank Dr. Xiaolong Li at beamline BL14B1 (Shanghai Synchrotron Radiation Facility) for assistance with the GIWAXS experiments. Aberration-corrected TEM was carried out at the Center for Functional Nanomaterials, Brookhaven National Laboratory, which is supported by the U.S. Department of Energy. Use of the Advanced Photon Source at Argonne National Laboratory was supported by the U.S. Department of Energy, Office of Science, Office of Basic Energy Sciences, under Contract No. DE-AC02-06CH11357. Part of this work (XAS data collection) was carried out at Stanford Synchrotron Radiation Lightsource, SLAC National Accelerator Laboratory, supported by the U.S. Department of Energy, Office of Science, Office of Basic Energy Sciences under Contract No. DE-AC02-76SF00515. XAS studies were performed with support of the Office of Science, OBES, Division of Chemical Sciences, Geosciences, and Biosciences (CSGB) of the DOE under contract no. DE-AC02-05CH11231 (J.Y.). We thank Dr. Charles Settens for assistance with in situ X-ray diffraction measurements. Part of the characterization and device fabrication was performed at the Harvard Center for Nanoscale Systems (CNS), a member of the National Nanotechnology Infrastructure Network (NNIN), which is supported by the National Science Foundation under NSF award no. ECS-0335765 This work used the Extreme Science

and Engineering Discovery Environment (XSEDE), which is supported by the National Science Foundation grant number ACI-1053575.

■ REFERENCES

- (1) Sun, L.; Campbell, M. G.; Dincă, M. *Angew. Chem., Int. Ed.* **2016**, *55*, 3566–3579.
- (2) Miner, E. M.; Fukushima, T.; Sheberla, D.; Sun, L.; Surendranath, Y.; Dincă, M. *Nat. Commun.* **2016**, *7*, 10942.
- (3) (a) Clough, A. J.; Yoo, J. W.; Mecklenburg, M. H.; Marinescu, S. C. *J. Am. Chem. Soc.* **2015**, *137*, 118–121. (b) Zhao, S.; Wang, Y.; Dong, J.; He, C.-T.; Yin, H.; An, P.; Zhao, K.; Zhang, X.; Gao, C.; Zhang, L.; Lv, J.; Wang, J.; Zhang, J.; Khattak, A. M.; Khan, N. A.; Wei, Z.; Zhang, J.; Liu, S.; Zhao, H.; Tang, Z. *Nat. Energy* **2016**, *1*, 16184.
- (4) Aubrey, M. L.; Long, J. R. *J. Am. Chem. Soc.* **2015**, *137*, 13594–13602.
- (5) Zhang, Z.; Yoshikawa, H.; Awaga, K. *J. Am. Chem. Soc.* **2014**, *136*, 16112–16115.
- (6) Campbell, M. G.; Sheberla, D.; Liu, S. F.; Swager, T. M.; Dincă, M. *Angew. Chem., Int. Ed.* **2015**, *54*, 4349–4352.
- (7) Campbell, M. G.; Liu, S. F.; Swager, T. M.; Dincă, M. *J. Am. Chem. Soc.* **2015**, *137*, 13780–13783.
- (8) Erickson, K. J.; Leonard, F.; Stavila, V.; Foster, M. E.; Spataru, C. D.; Jones, R. E.; Foley, B. M.; Hopkins, P. E.; Allendorf, M. D.; Talin, A. A. *Adv. Mater.* **2015**, *27*, 3453–3459.
- (9) Sheberla, D.; Bachman, J. C.; Elias, J. S.; Sun, C.; Shao-Horn, Y.; Dincă, M. *Nat. Mater.* **2017**, *16*, 220–224.
- (10) AlKaabi, K.; Wade, C. R.; Dincă, M. *Chem.* **2016**, *1*, 264–272.
- (11) Wu, G.; Huang, J.; Zang, Y.; He, J.; Xu, G. *J. Am. Chem. Soc.* **2017**, *139*, 1360–1363.
- (12) Sheberla, D.; Sun, L.; Blood-Forsythe, M. A.; Er, S.; Wade, C. R.; Brozek, C. K.; Aspuru-Guzik, A.; Dincă, M. *J. Am. Chem. Soc.* **2014**, *136*, 8859–8862.
- (13) Kambe, T.; Sakamoto, R.; Kusamoto, T.; Pal, T.; Fukui, N.; Hoshiko, K.; Shimojima, T.; Wang, Z.; Hirahara, T.; Ishizaka, K.; Hasegawa, S.; Liu, F.; Nishihara, H. *J. Am. Chem. Soc.* **2014**, *136*, 14357–14360.
- (14) Huang, X.; Sheng, P.; Tu, Z.; Zhang, F.; Wang, J.; Geng, H.; Zou, Y.; Di, C.-A.; Yi, Y.; Sun, Y.; Xu, W.; Zhu, D. *Nat. Commun.* **2015**, *6*, 7408.
- (15) Chen, S.; Dai, J.; Zeng, X. C. *Phys. Chem. Chem. Phys.* **2015**, *17*, 5954–5958.
- (16) Yamada, M. G.; Soejima, T.; Tsuji, N.; Hirai, D.; Dincă, M.; Aoki, H. *Phys. Rev. B: Condens. Matter Mater. Phys.* **2016**, *94*, 081102.
- (17) Wu, M.; Wang, Z.; Liu, J.; Li, W.; Fu, H.; Sun, L.; Liu, X.; Pan, M.; Weng, H.; Dincă, M.; Fu, L.; Li, J. *2D Mater.* **2017**, *4*, 015015.
- (18) Lahiri, N.; Lotfizadeh, N.; Tsuchikawa, R.; Deshpande, V. V.; Louie, J. J. *J. Am. Chem. Soc.* **2017**, *139*, 19–22.
- (19) Chisnell, R.; Helton, J. S.; Freedman, D. E.; Singh, D. K.; Bewley, R. I.; Nocera, D. G.; Lee, Y. S. *Phys. Rev. Lett.* **2015**, *115*, 147201.
- (20) Sun, L.; Park, S. S.; Sheberla, D.; Dincă, M. *J. Am. Chem. Soc.* **2016**, *138*, 14772–14782.
- (21) Kobayashi, H.; Cui, H.; Kobayashi, A. *Chem. Rev.* **2004**, *104*, 5265–5288.
- (22) Beloborodov, I. S.; Lopatin, A. V.; Vinokur, V. M.; Efetov, K. B. *Rev. Mod. Phys.* **2007**, *79*, 469–518.
- (23) Cho, E.; Risko, C.; Kim, D.; Gysel, R.; Miller, N. C.; Breiby, D. W.; McGehee, M. D.; Toney, M. F.; Kline, R. J.; Brédas, J.-L. *J. Am. Chem. Soc.* **2012**, *134*, 6177–6190.
- (24) Stassen, I.; Burtch, N.; Talin, A.; Falcaro, P.; Allendorf, M.; Ameloot, R. *Chem. Soc. Rev.* **2017**, *46*, 3185–3241.

■ NOTE ADDED IN PROOF

A publication on a similar topic appeared while this manuscript was under review. See: Clough, A. J.; Skelton, J. M.; Downes, C. A.; De la Rosa, A.; Yoo, J. W.; Walsh, A.; Melot, B. C.; Marinescu, S. C. *J. Am. Chem. Soc.* **2017**, *139*, 10863–10867.

Supporting Information

Signature of Metallic Behavior in the Metal-Organic Frameworks $M_3(\text{hexaiminobenzene})_2$ ($M = \text{Ni}, \text{Cu}$)

Jin-Hu Dou,[†] Lei Sun,[†] Yicong Ge,[†] Wenbin Li,[‡] Christopher H. Hendon,[†] Ju Li,[§] Sheraz Gul,[⊥] Junko Yano,[⊥] Eric A. Stach,[#] and Mircea Dincă^{*,†}

[†]Department of Chemistry, Massachusetts Institute of Technology, 77 Massachusetts Avenue, Cambridge, Massachusetts 02139, United States

[‡]Research Laboratory of Electronics, Massachusetts Institute of Technology, 77 Massachusetts Avenue, Cambridge, Massachusetts 02139, United States

[§]Department of Nuclear Science and Engineering, Department of Materials Science and Engineering, Massachusetts Institute of Technology, 77 Massachusetts Avenue, Cambridge, Massachusetts 02139, United States

[⊥]Molecular Biophysics and Integrated Bioimaging Division, Lawrence Berkeley National Laboratory, Berkeley, California 94720, United States

[#]Center for Functional Nanomaterials, Brookhaven National Laboratory, Upton, New York 11973, United States

*mdinca@mit.edu

Table of Contents

1. General procedures and experimental details
2. Device fabrication and characterization
3. Computational methods
4. Synthetic procedures and characterization
5. Figures S1-21
6. References

1. General procedures and experimental details

All commercially available chemicals were used without further purification unless otherwise noted. All air and water sensitive reactions were performed under a nitrogen atmosphere. Column chromatography was performed with silica gel. All yields refer to isolated yields. ^1H and ^{13}C NMR spectra were recorded on Bruker AVANCE III spectrometers 500 MHz. All chemical shifts are reported in parts per million (ppm). DMSO- d_6 (2.50 ppm) is the reference for ^1H NMR chemical shifts, and DMSO- d_6 (39.52 ppm) is the reference for ^{13}C NMR chemical shifts.

Mass spectra were recorded on a Bruker Apex IV Fourier Transform Ion Cyclotron Resonance Mass Spectrometer.

The nitrogen adsorption measurements were performed on a Micromeritics ASAP 2020 Surface Area and Porosity Analyzer. An oven-dried sample tube equipped with a TranSealTM (Micromeritics) was evacuated and tared. The sample was transferred to the sample tube, which was then capped with a TranSealTM. The sample was heated to 120 °C, as determined by thermogravimetric analysis, under a dynamic vacuum of 4 mtorr until the outgas rate was less than 2 mtorr/minute. The evacuated sample tube was weighed again and the sample mass was determined by subtracting the mass of the previously tared tube. The N₂ isotherm was measured using a liquid nitrogen bath (77 K). Ultrahigh purity grade (99.999% purity) N₂, oil-free valves and gas regulators were used for all the free space correction and measurement.

Powder X-ray diffraction (PXRD) patterns were obtained at beamline 11-BM of the Advanced Photon Source (APS), using a wavelength of 0.517045 Å. Diffraction patterns were collected at 100 K and 295 K, respectively. Data points were collected every 0.001° (2 θ step) in a range from -6.5 to 28°. Background of PXRD patterns were corrected by Bruker Diffrac. Suite EVA software. The unit cell parameters were determined directly from the synchrotron PXRD pattern by TREOR, and the diffraction intensities were extracted by Le Bail fitting using JANA2006. *In situ* PXRD patterns were obtained on a Rigaku Smartlab using a wavelength of 1.5405 Å. The samples were mounted onto the substrate holder of a variable-temperature chamber, and was kept in dynamic vacuum. The background of the PXRD patterns was corrected using the Bruker Diffrac.Suite EVA software.

Elemental analyses were performed by Robertson Microlit Laboratories, Ledgewood NJ.

Transmission electron microscopy (TEM) images were obtained with a spherical aberration corrected FEI Titan 80/300, operated at an accelerating voltage of 300 kV at BNL. Samples were drop-cast onto Cu TEM grids from powder dispersed in methanol.

X-ray absorption spectroscopy (XAS) measurements were conducted at the Ni and Cu K-edges at the Stanford Synchrotron Radiation Lightsource (SSRL) using beamline 7-3. The storage ring was operating with an average ring current of 500 mA at 3.0 GeV. The beamline is equipped with a cryogenically cooled Si (220) double-crystal monochromator which was detuned to 50% of flux maximum at Ni/Cu K-edge to minimize harmonics. Incident and transmitted X-ray flux was monitored using N₂-filled ion chambers (I_0 , in front of the sample and I_1 after the sample). Absorption data was collected in transmission mode and samples were diluted with boron nitride to achieve the concentration needed to yield a desired edge step-height (~0.4-0.7) for the absorption edge of interest. The diluted samples were packed in 0.5 mm thick aluminum sample holders sealed with Kapton film windows on both sides. Energy calibration was accomplished by the first peak maximum of first derivative of Ni foil

(8333.0 eV) and Cu foil (8980.3 eV), placed between two N₂-filled ion chambers (*I*₁ and *I*₂) downstream of the sample. All data were collected at room temperature and spectra were closely monitored for radiation damage.

The data were reduced with standard procedures using SamView (SixPack software, <http://www.sams-xrays.com/sixpack>). Pre-edge and post-edge backgrounds were subtracted from the XAS spectra using Athena (Demeter version 0.9.25),¹ and results were normalized with respect to the edge height. Background in *k*-space was removed through a five-domain cubic spline. The extracted *k*-space data, $k^3\chi(k)$, was then Fourier transformed into *r*-space (Figure S10), where the *k*-ranges were 3.0-12.6 Å⁻¹ for Ni, and 3.8-12.8 Å⁻¹ for Cu. Note that in EXAFS data, peaks are shifted to a lower *r* value as compared to the actual pair distances due to phase shift. EXAFS curve fitting was performed using Artemis (Demeter software version 0.9.25) where *ab initio* calculated phases and amplitudes were determined using program FEFF6² and crystal structure information obtained from XRD. The coordination number was fixed during the fitting whereas bond distances (R) and mean square displacement of the bond distances (σ^2) were varied. The values for S_0^2 , the amplitude reduction factor, were determined from the fits to the data of nickel(II) phthalocyanine and copper(II) phthalocyanine, and were fixed (0.80 for Ni and 0.85 for Cu data) during the fits. The fits were carried out in *r*-space, with R' (apparent distance) ranging from 1.0-3.8 Å for Ni and 1.0-4.0 Å for Cu. The best fits and corresponding data are presented in Figure S10 along with the best fit parameters listed in the tables shown as insets. Along with the first three in-plane shells, Ni-Ni/Cu-Cu paths from the adjacent layers were needed to fit the data. Note that only half of the metal sites have metal neighbors from adjacent layers (Figure S10). In addition, in-plane multiple scattering paths and the nearest Ni-N/Cu-N path from adjacent layers were included to improve the fit quality.

The 2D grazing incident wide-angle X-ray scattering (GIWAXS) data were obtained at beamline BL14B1 of the Shanghai Synchrotron Radiation Facility (SSRF) at a wavelength of 1.2398 Å. BL14B1 is a beamline based on a bending magnet and a Si (111) double crystal monochromator. The size of the focus spot is approximately 0.5 mm and the end station is equipped with a Huber 5021 diffractometer. A NaI scintillation detector was used for data collection.

X-ray photoelectron spectroscopy (XPS) was performed at the Harvard Center for Nanoscale Systems (Cambridge, MA, USA) on a Thermo Scientific K-Alpha system equipped with an Al source and 180° double focusing hemispherical analyzer and 128-channel detector using a 400 μm X-ray spot size.

Ultraviolet photoemission spectroscopy (UPS) was conducted on a Kratos AXIS Ultra-DLD Photoelectron Spectrometer under an ultrahigh vacuum of about 3×10^{-9} Torr with an unfiltered He I gas discharge lamp source (21.22 eV) at 300 K. For UPS measurements, the samples were biased at -9 V to observe the low-energy secondary electron cutoff. The instrumental energy resolution for UPS was 0.1 eV. Before measurements, MOF films were transferred onto highly doped conductive silicon substrates (1.0 × 1.0 cm²). The high electrical conductivity of both MOF films and the substrates eliminated charging effects, which was proven by the observation that multiple successive UPS measurements did not change the shape and position of the UPS spectra and only improved the signal-to-noise ratio. UPS was chosen to study the density of states close to the Fermi level instead of XPS because UPS has higher sensitivity and resolution in this energy range.

Thermogravimetric analysis (TGA) was performed on a TA Instruments Q500

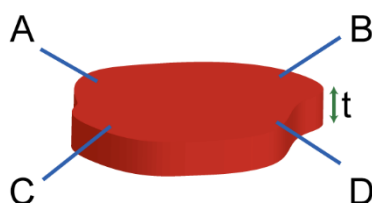
Thermogravimetric Analyzer at a heating rate of 1 °C/min under a nitrogen gas flow of 10 mL/min on a platinum pan.

Scanning electron microscopy (SEM) was conducted at the Harvard Center for Nanoscale Systems (Cambridge, MA, USA) on a Leo Supra 55VP FEG SEM or on a Zeiss Ultra 55 SEM with an InLens detector and an operating voltage of 3 kV. Optical microscopy (OM) images were obtained by Leica S6 E stereoscopic microscope.

2. Device fabrication and characterization

Van der Pauw method for pressed pellets³

Pressed pellets were made by adding a sample of the MOF into a 6 mm inner-diameter trapezoidal split sleeve pressing die (Across International) and pressing the die set by a hydraulic pump (MTI corporation) for 15 min. The applied pressure was approximately 1 GPa. The thickness of the pellet was measured by a micrometer (Mitutoyo). The pellet (or a piece of the pellet with no observable cracks) was placed onto a piece of dry aluminum oxide. Four gold wires (Alfa Aesar, 25 μm in diameter) were pasted onto the four corners of the pellet using carbon paste (Electron Microscopy Sciences), and the other ends of the gold wires were pasted onto the aluminum oxide slide using carbon paste. The configuration of probes is shown below (Scheme S1). The device was mounted onto the sample chuck of a probe station (Janis Cryogenics ST-500) with thermally conductive and electrically insulating grease (DuPont Krytox). This probe station is equipped with four micro-manipulators that allowed us to control the positions of the probes with a resolution of 5 μm . Copper wires (100 μm in diameter) were used as probes, and were connected to the carbon paste pads on the aluminum oxide slide by additional carbon paste. The device was kept in air for 2 h to ensure that the carbon paste was completely dry.



Scheme S1. Schematic depiction of the van der Pauw arrangement of probes. Red solid represents the pressed pellet, and blue lines represent probes.

The temperature of the device was equilibrated by the heater of the probe station chuck and liquid nitrogen, and was controlled by a temperature controller (Scientific Instrument model 9700). Probes were connected to a sourcemeter (Keithley model 2450) through triax cables (Keithley model 7078-TRX-10). The chamber of the probe station was covered by a stainless steel lid. This lid has a quartz window in the center, which was covered by a black plastic to keep the device in the dark. The probe station was evacuated by a diaphragm pump and a turbo pump. The pressure reached $\sim 1 \times 10^{-5}$ torr after 1 h evacuation and the pumps were kept running with full power. With a home-made LabView program, we collected an I-V curve every minute by scanning the current from 100 μA to $-100 \mu\text{A}$ with a step size of 20 μA , speed of 5 number of power line circles (NPLC), and delay time of 2 ms, and measuring voltage at each step. We supplied current from probe A and B and measured voltage from probes C and D. The electrical resistance (R_{AB}) was extracted from linear regression results of the I-V curve. While monitoring the electrical resistance of the pellet, we kept the pellet at 420 °C for three days. Its electrical resistance kept decreasing during this time likely because

annealing reduced grain boundaries, and finally leveled off. Then we cooled down the pellet from 420 to 200 K, with 10 K per step and 30 min for each step. The electrical resistance remained constant at the end of each step, indicating thermal equilibrium was reached. Therefore, we considered the last result of each step as the electrical resistance of the pellet.

After various-temperature electrical resistance measurement, we kept the pellet at 300 K for 6 h, and performed van der Pauw electrical conductivity measurements. The pellet was kept in vacuum ($\sim 1 \times 10^{-5}$ torr) and in the dark. We scanned current from 100 μA to $-100 \mu\text{A}$ with a step size of 10 μA , speed of 10 NPLC, and delay time of 2 ms, and measured voltage at each step. The electrical resistance was extracted from linear regression results of the I-V curve. We first supplied current from probes A and B and measured voltage from probes C and D to obtain electrical resistance R_{AB} , and then change cable connections to obtain R_{AC} . Electrical conductivity was calculated based on R_{AB} , R_{AC} , and pellet thickness (t) with the method discussed in Reference S1. Assuming R_{AB} scaled with electrical conductivity, the electrical conductivity at other temperatures was normalized to the value at 300 K, giving rise to the data shown in Figure 4a.

3. Computational methods

The molecular charge-neutral hexaaminobenzene was optimized by GAMESS-US within the DFT construct with the B3LYP functional and a suitably large basis, 6-311+G(d). Three terminal metals (Ni or Cu) were then introduced to the singly deprotonated ligand and a further geometry optimization was performed. The resultant structure was then tiled periodically to form a hexagonal structure, shown in Figure S12, with cell length $a = b = 13.48$ Å for the Ni and Cu frameworks, respectively. In both cases case, metal–ligand distances were initially constructed using the single molecule values from the optimized fragment.

The interlayer spacing (c direction) was empirically obtained from fitting the simulated PXRD to the experimentally measured trace. To assess the slipped plane nature of the framework, one layer was kept fixed, while the second layer was translated to a total of 82 unique geometries. DFT single-point energy calculations were carried out on all 82 of these structures using the PBE (Perdew-Burke-Ernzerhof) exchange-correlation functional with Grimme's D2 dispersion correction as implemented in VASP. A kinetic energy cutoff of 400 eV and a Γ -centered $2 \times 2 \times 6$ \mathbf{k} -point mesh was used for all calculations. The self-consistent energy of each of these structures was then used as a sample point for the energy of a potential energy surface that was interpolated using 2D Lagrange polynomials over a tensor product grid of Chebyshev points which were subsequently mapped back to the grid of original translations. Interpolation over the finer grid is expected to yield a more accurate representation of the potential energy surface in the region. The minimum of the potential energy surface corresponds to a displacement of ~ 1.8 - 1.9 Å along the a and/or b axis.

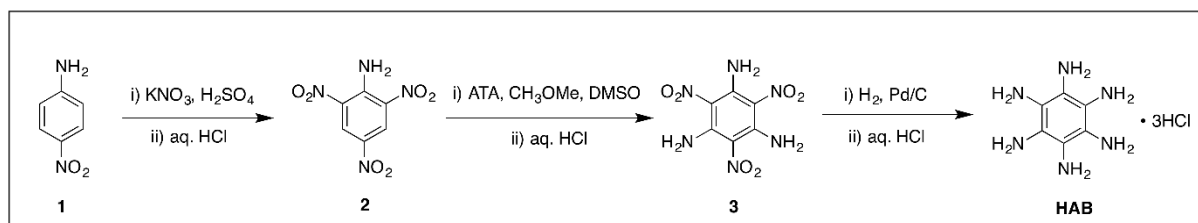
The resultant unit cells corresponded to the $Cmcm$ and $C222_1$ space groups for the Ni and Cu frameworks, respectively.

Electronic band structures were then computed in VASP using the hybrid-GGA functional HSE06 with a 500 eV cutoff and Γ -centered \mathbf{k} -point sampling along high symmetry vectors (detailed in Figure 3). The Γ -only projected density of state (pDOS) is presented to deconvolute the band structure contributions.

4. Synthetic procedures and characterization

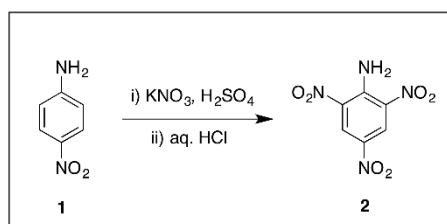
The compounds **1** and 4-amino-1,2,4-triazole (ATA) are commercially available from *Sigma Aldrich*. The compound hexaaminobenzene (HAB) and its precursors were synthesized according to the literature.⁴

Overview



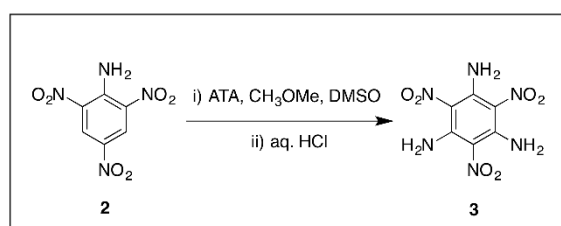
*Warning: Compounds 2,4,6-trinitroaniline (TNA) **2** and 1,3,5-triamino-2,4,6-trinitrobenzene (TATB) **3** are very sensitive to mechanical force and highly explosive under alkaline conditions. Both should be handled with extreme caution.*

Synthesis of HAB



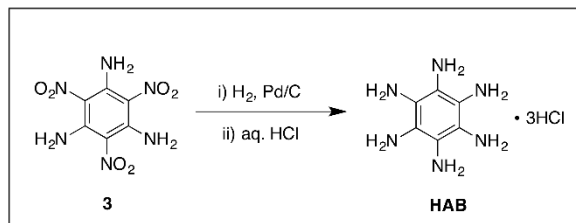
2,4,6-trinitroaniline (TNA) **2**

4-Nitroaniline (20 g, 0.144 mol) **1** and H_2SO_4 (100 mL) were charged in a round-bottom flask. A solution of KNO_3 (70 g, 0.70 mol) in H_2SO_4 (100 mL) was then added dropwise at 50 °C. The mixture was heated to 80 °C for 3 h and 110 °C for 3 h. After completion of the reaction, the reaction mixture was cooled to ambient temperature and poured into ice water. The precipitates were collected by suction filtration, air-dried, and recrystallized from 0.4 M aq. HCl solution to give 16.5 g (49.9% yield) of 2,4,6-trinitroaniline (glassy light yellow crystal); MS (ESI, DIP): $m/z = 227.9898$ [$\text{M} - \text{H}$]⁻. ¹H NMR (400 MHz, DMSO): $\delta = 8.59$ (2H), 5.21 (6H) ppm. ¹³C NMR (100 MHz, DMSO): δ 160.61, 141.84, 125.19, 124.41 ppm. ESI-HRMS calcd. for $\text{C}_6\text{H}_4\text{N}_4\text{O}_6$ ([M]): 228.01; Found: 227.9898.



1,3,5-triamino-2,4,6-trinitrobenzene (TATB) **3**

NaOMe (23.8 g, 0.44 mol) was added to a solution of TNA (4.56 g, 0.02 mol) and ATA (16.8 g, 0.2 mol) in DMSO (300 mL). The reddish orange suspension was stirred at ambient temperature for 3 h. The reaction mixture was then poured into cold aq. HCl (0.4 M) solution. The resulting precipitates were collected by suction filtration, washed with distilled H₂O and dried. The solid was dissolved in DMSO with small amounts of NaOH with gentle heating up to 70 °C, when the compound was completely dissolved the solution was poured into ice-cold aq. HNO₃ (0.4 M) solution. The precipitate was again collected by filtration to give 4.62 g (89.5% yield) of TATB (deep yellow powder); ¹³C NMR (100 MHz, DMSO): 157.09, 146.60, 117.31, 112.85 ppm. ESI-HRMS calcd. for C₆H₆N₆O₆ ([M]): 258.03; Found: 258.0154.



Hexaaminobenzene (HAB)

TATB (3.0 g, 0.012 mol) was taken into a high-pressure hydrogenation bottle with 10% Pd/C (500 mg) and pure EtOAc (150 mL). The reaction flask was fixed on a hydrogenation apparatus and agitated under H₂ (4.2 bar) until all the yellowish color of the reactant disappeared completely within 3 d. Then, concentrated HCl (90 mL) was added, and the reaction was continued under H₂ for additional 5 h. The reaction mixture was filtered under reduced pressure over Celite to remove Pd/C. HAB trihydrochloride crystallized out in high yield. The precipitates were collected by suction filtration with a polytetrafluoroethylene (PTFE) membrane (0.5 μm pore size) and dried in an oven at 70 °C for 2 h under reduced pressure. The white small crystals were re-dissolved in deionized H₂O and filtered through a PTFE membrane to remove solid impurities. 80 mL of concentrated aq. HCl solution was added into a flask containing the filtrate. The flask was tightly sealed and placed in a freezer until the formation of large crystals. The crystals were collected on a PTFE membrane filter in the gravity filtration, washed thoroughly with EtOAc, and dried in a vacuum oven to afford 3.0 g (93.2% yield), (see Figure S1). ¹H NMR (400 MHz, DMSO): δ = 9.52 (12H) ppm. ESI-HRMS calcd. for C₆H₁₃N₆ ([M+H]⁺): 168.11; Found: 169.1196.

Synthesis of Ni₃(HIB)₂ (HIB = hexaiminobenzene) powder

A solution of 32 mg of Ni(NO₃)₂·6H₂O (0.11 mmol) and 0.7 mL of 14M NH₄OH in 3 mL of degassed DMSO was added to a solution of 20 mg of HAB·3HCl (0.072 mmol) in 3 mL degassed DMSO in a 20 mL scintillation vial. The vial was loosely capped and put under 65°C for 2 hours without stirring. The product precipitated out as black solids. The mixture was centrifuged, decanted and washed with deionized water twice and acetone once. The solid product was dried under vacuum on a Schlenk line for 10 minutes. C, H, N, and Ni microelemental analysis for Ni₃(C₆H₆N₆)₂: Calculated: C: 28.80%; H: 2.42%; N: 33.59%; Ni: 35.19%. Found: C: 28.68%; H: 2.26%; N: 33.53%; Ni(ICP-OES): 35.47%.

Synthesis of Cu₃(HIB)₂ powder

A solution of 27 mg of CuSO₄·5H₂O (0.11 mmol) and 0.7 mL of 14M NH₄OH in 3 mL of degassed DMSO was added to a solution of 20 mg of HAB·3HCl (0.072 mmol) in 3 mL degassed DMSO in a 20 mL scintillation vial. The vial was loosely capped and kept at 65°C in air for 2 hours without stirring. The product precipitated out as black solids. The mixture

was centrifuged, decanted and washed with deionized water twice and acetone once. The solid product was dried under vacuum on a Schlenk line for 10 minutes. C, H, N, and Cu microelemental analysis for $\text{Cu}_3(\text{C}_6\text{H}_6\text{N}_6)_2$: Calculated: C: 27.99%; H: 2.35%; N: 32.64%; Cu: 37.02%. Found: C: 27.76%; H: 2.15%; N: 32.45%; Cu(ICP-OES): 37.19%.

Synthesis of $\text{Ni}_3(\text{HIB})_2$ film

In a glove box with nitrogen atmosphere, 50 μL of deoxygenated ethylenediamine was added to a solution of 28.2 mg of $\text{Ni}(\text{NO}_3)_2 \cdot 6\text{H}_2\text{O}$ (0.097 mmol) in 3 mL of deoxygenated water. The mixture was added to a solution of 17.5 mg of $\text{HAB} \cdot 3\text{HCl}$ (0.063 mmol) dissolved in 3 mL of deoxygenated water in a 30 mL beaker. The beaker was sealed with fine-meshed Parafilm[®] and put into a 50 mL glass jar, which is capped and sealed also by Parafilm[®]. The jar was taken out of the glove box into a fume hood. After standing for 12 hours at 40 °C, the MOF film emerged at the gas-liquid interface (see Figure S17). The film was washed by deionized water twice and isopropyl alcohol once.

Synthesis of $\text{Cu}_3(\text{HIB})_2$ film

In a glove box with nitrogen atmosphere, 40 μL of deoxygenated ethylenediamine was added to a solution of 24.1 mg of $\text{CuSO}_4 \cdot 5\text{H}_2\text{O}$ (0.097 mmol) in 3 mL of deoxygenated water. The mixture was added to a solution of 17.5 mg of $\text{HAB} \cdot 3\text{HCl}$ (0.063 mmol) dissolved in 3 mL of deoxygenated water in a 30 mL beaker. The beaker was sealed with fine-meshed Parafilm[®] and put into a 50 mL glass jar, which is capped and sealed also by Parafilm[®]. The jar was taken out of the glove box into a fume hood. After standing for 12 hours at 40 °C, the MOF film emerged at the gas-liquid interface (see Figure S17). The films were obtained by immersing the Si wafer substrate into the reaction solution and passing through the air/aqueous interface horizontally and slowly, after the film formed. The film was washed by deionized water twice and isopropyl alcohol once.

5. Figures S1-21

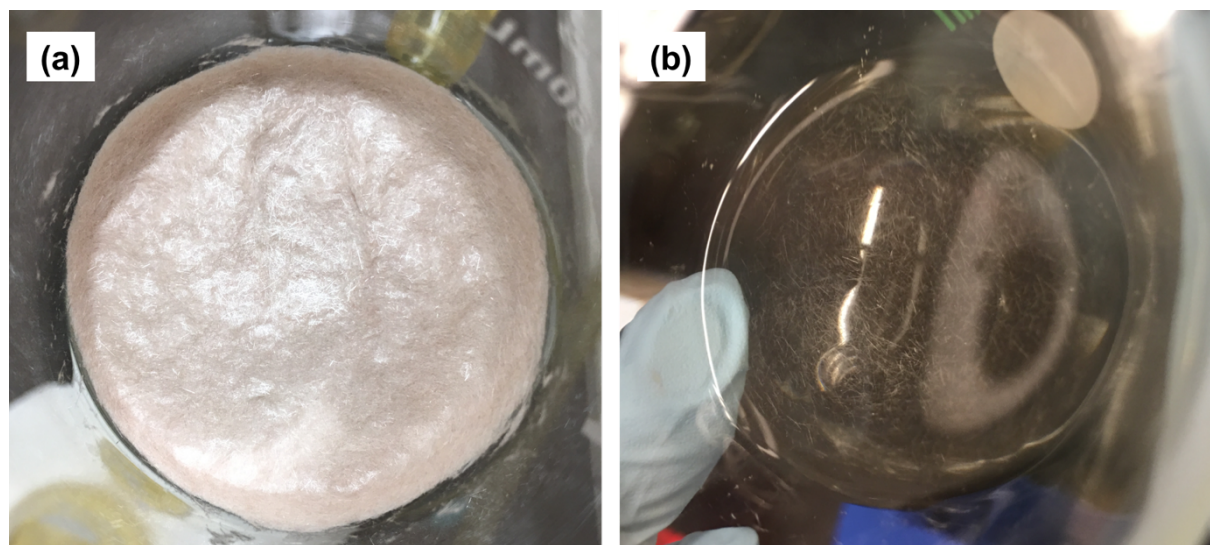


Figure S1. Needle-shaped light pink HAB·3HCl crystals (a) on a fine filter frit and (b) at the bottom of a flask.

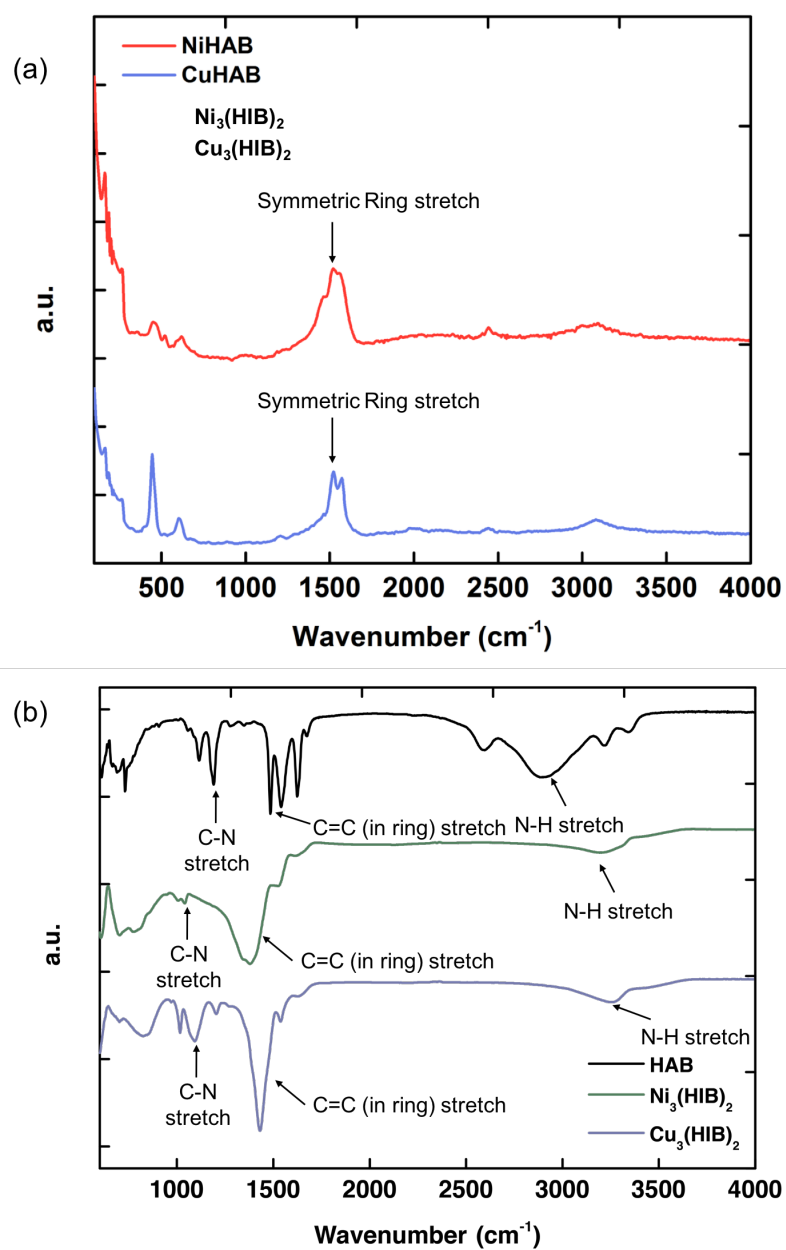


Figure S2. (a) Raman spectrum of $\text{Ni}_3(\text{HIB})_2$ (red) and $\text{Cu}_3(\text{HIB})_2$ (blue) powder. (b) IR spectrum of HAB (black), $\text{Ni}_3(\text{HIB})_2$ (green) and $\text{Cu}_3(\text{HIB})_2$ (blue) powder.

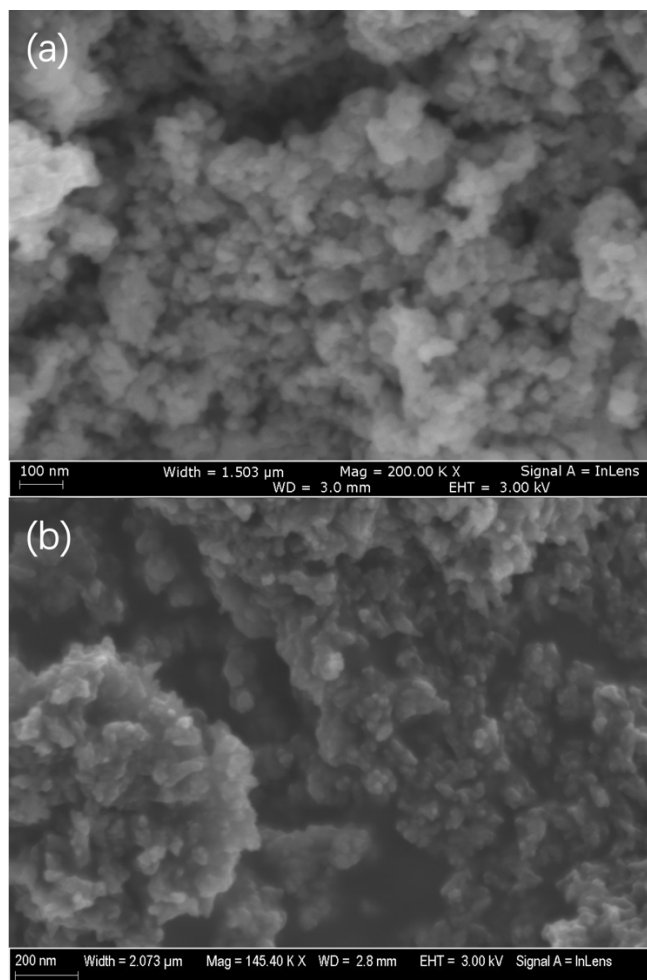


Figure S3. SEM images of (a) $\text{Ni}_3(\text{HIB})_2$ and $\text{Cu}_3(\text{HIB})_2$ powder.

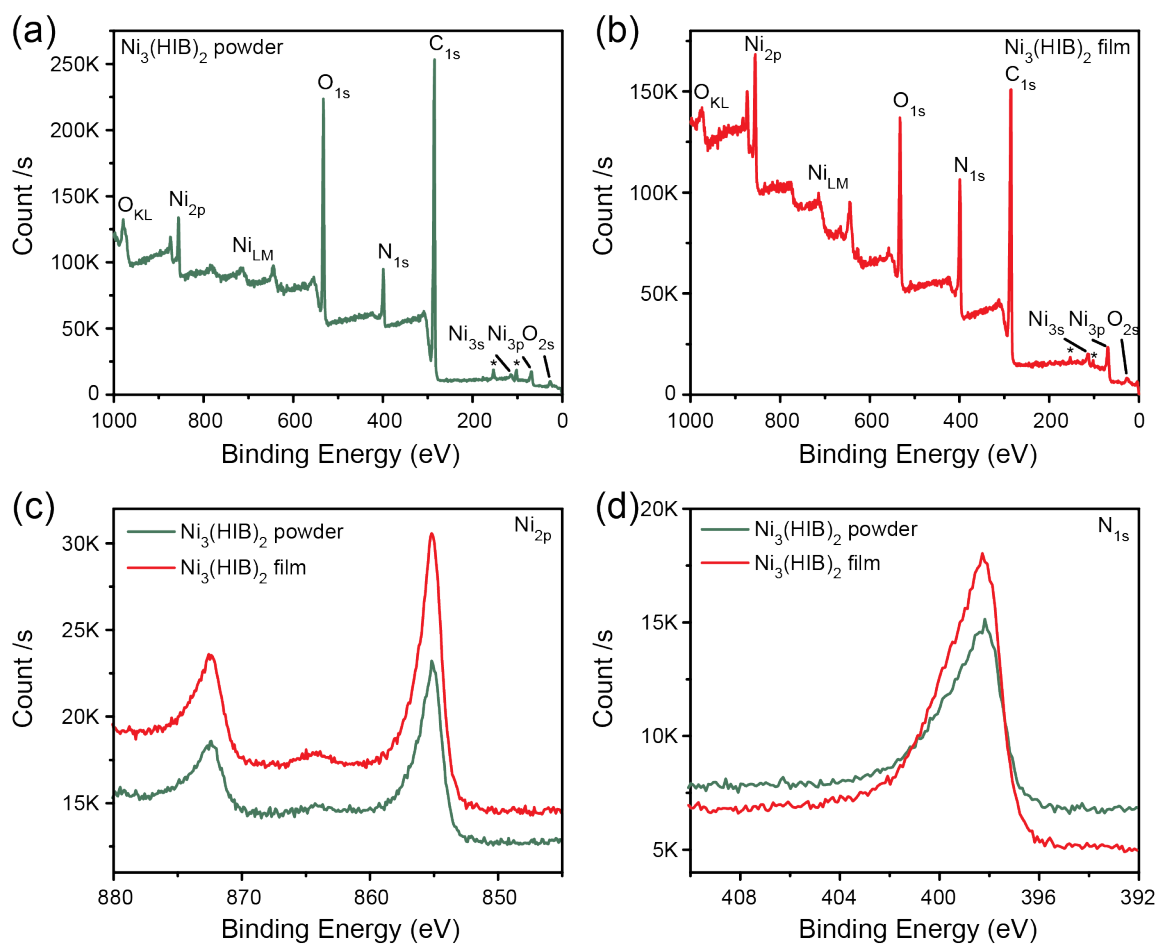


Figure S4. XPS spectra of $\text{Ni}_3(\text{HIB})_2$ powder (a) and film (b). (c) Ni(2p) region and (d) N(1s) region of $\text{Ni}_3(\text{HIB})_2$ powder (green) and film (red).

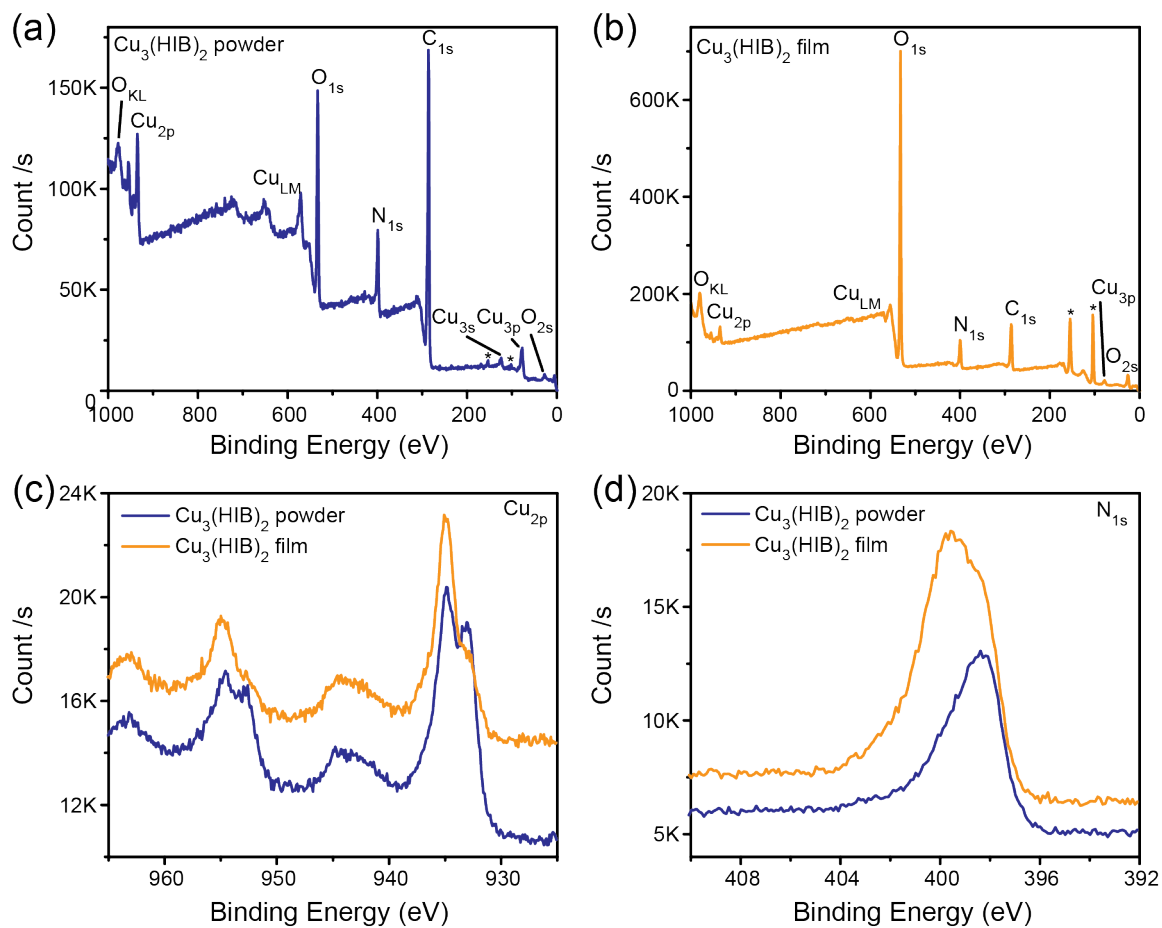


Figure S5. XPS spectra of $\text{Cu}_3(\text{HIB})_2$ powder (a) and film (b). (c) $\text{Cu}(2p)$ region and (d) $\text{N}(1s)$ region of $\text{Ni}_3(\text{HIB})_2$ powder (blue) and film (orange).

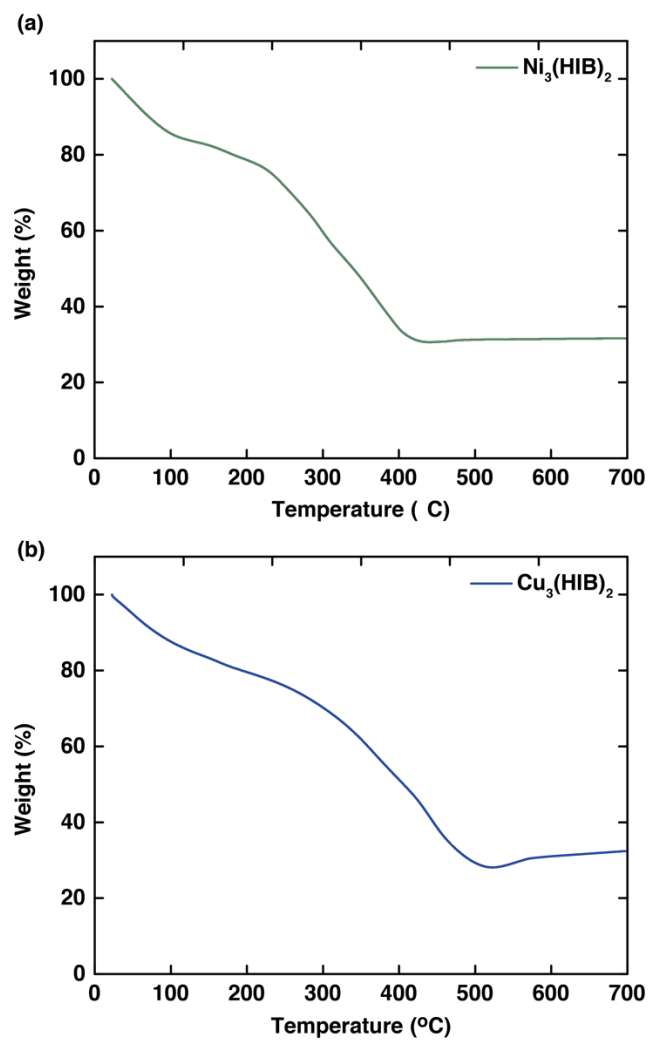


Figure S6. TGA traces of (a) $\text{Ni}_3(\text{HIB})_2$ powder and (b) $\text{Cu}_3(\text{HIB})_2$ powder collected at a heating rate of 1 °C/min under a nitrogen gas flow of 10 mL/min on a platinum pan.

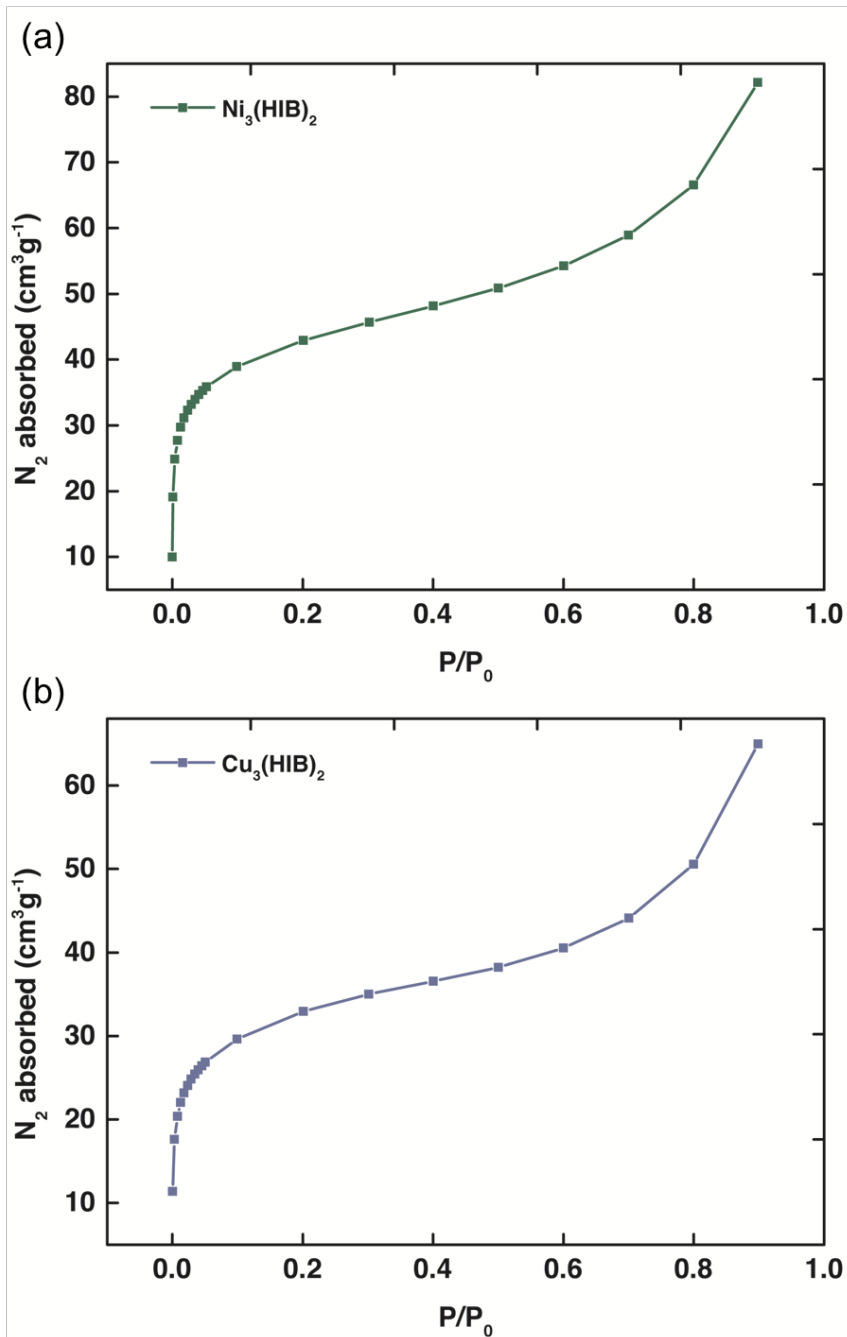


Figure S7. Nitrogen adsorption isotherms for (a) Ni₃(HIB)₂ and (b) Cu₃(HIB)₂. The isotherms were fit to the BET equation to give apparent BET surface areas of 151.5914 ± 0.9057 m²/g for Ni₃(HIB)₂ and 114.3221 ± 1.1855 m²/g for Cu₃(HIB)₂. The C values of the BET fitting are 401.662247 for Ni₃(HIB)₂ and 366.306536 for Cu₃(HIB)₂.

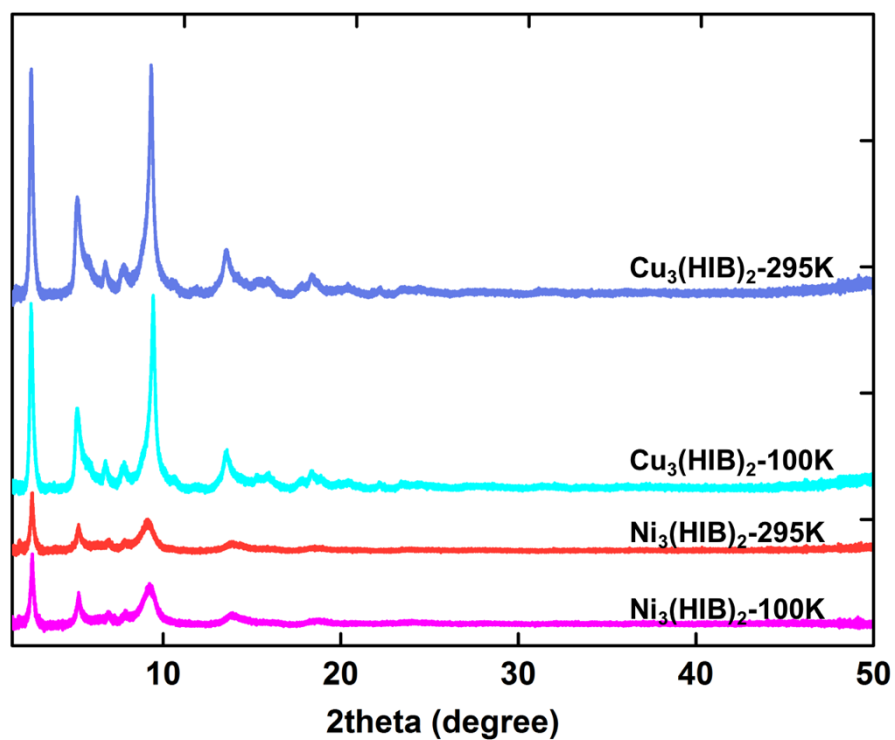


Figure S8. PXRD patterns of $\text{Cu}_3(\text{HIB})_2$ and $\text{Ni}_3(\text{HIB})_2$ powder samples at 295 K and 100 K, obtained at beamline 11-BM of the Advanced Photon Source (APS) using a wavelength of 0.517045 Å.

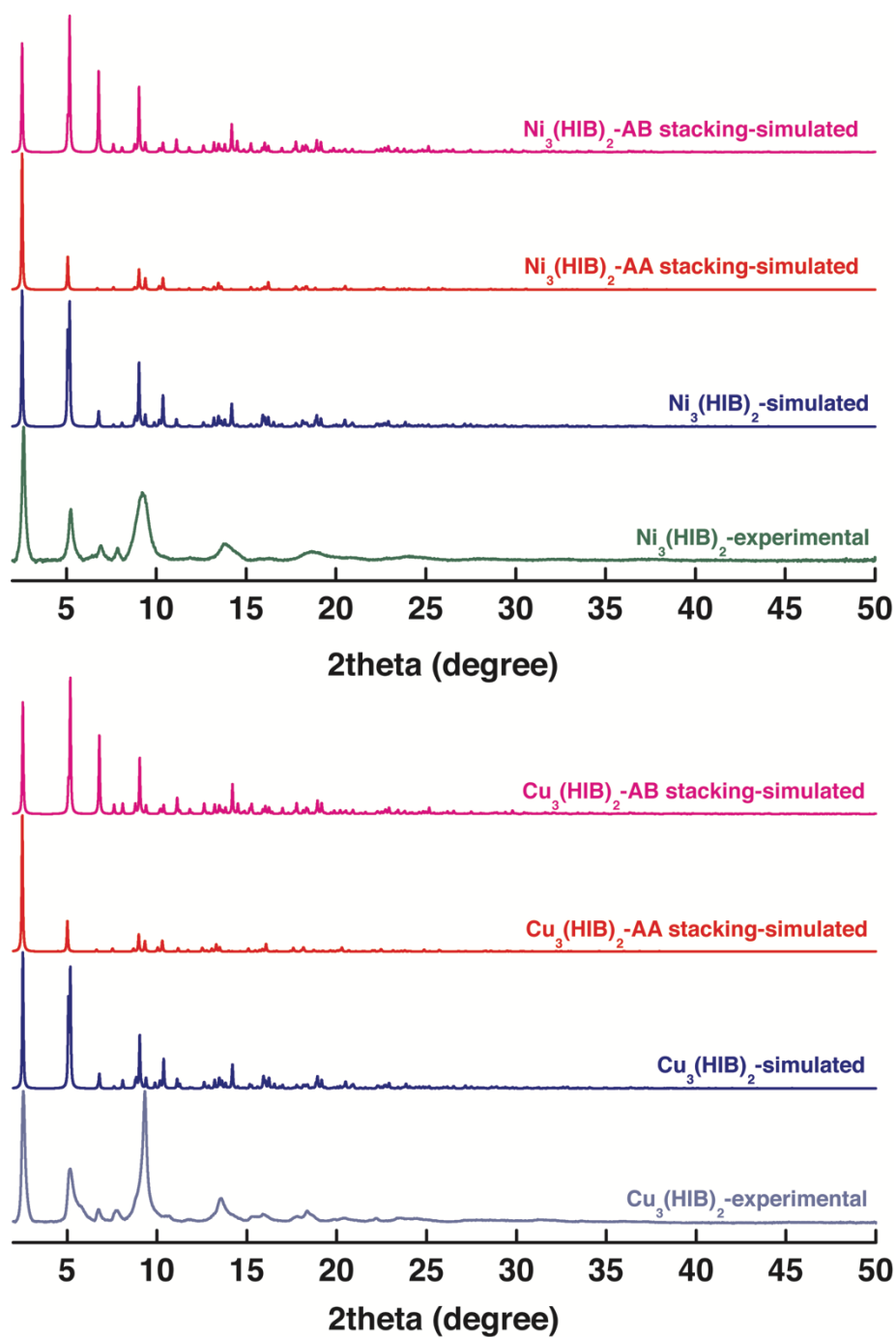


Figure S9. Experimental and simulated PXRD patterns of $M_3(\text{HIB})_2$. (“AA” stacking means eclipsed, “AB” stacking means staggered and “ $M_3(\text{HIB})_2$ -simulated” means slipped-parallel structure according to the experimental data.

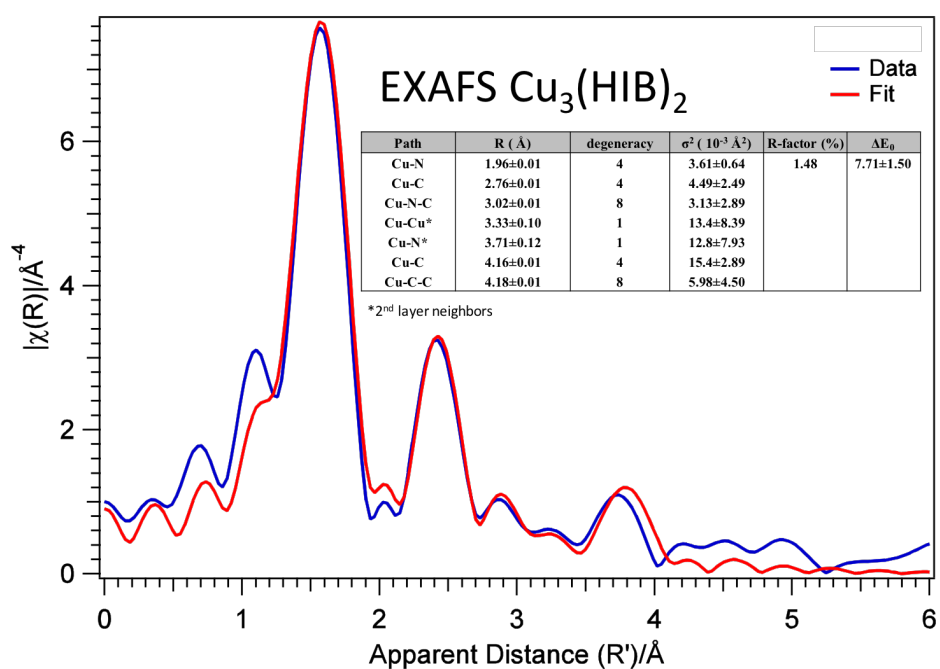
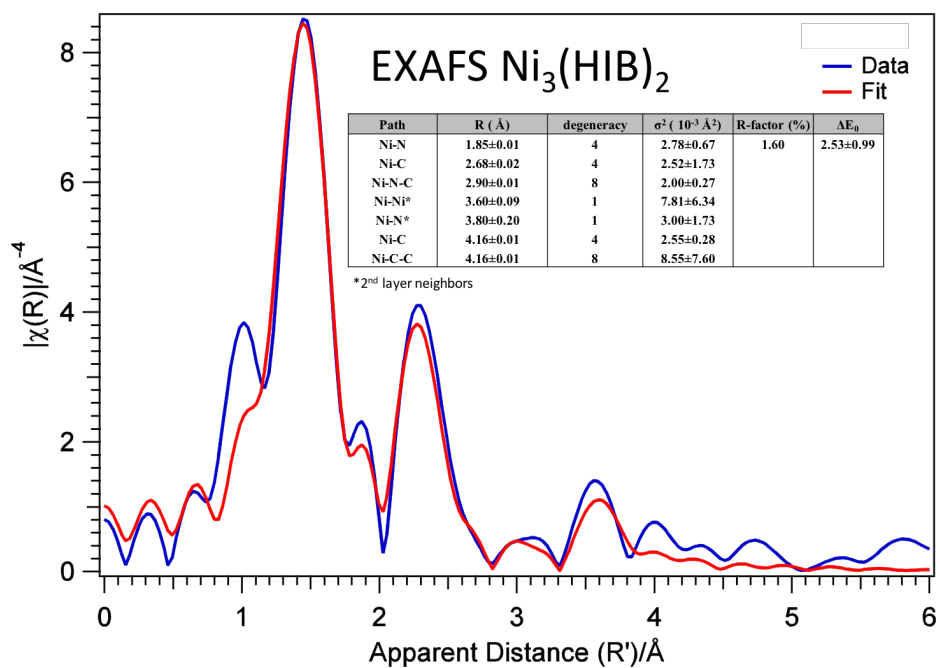


Figure S10. *r*-space Ni/Cu K-edge EXAFS data (blue) and fits (red) of M₃(HIB)₂. The best fit parameters are shown as insets.

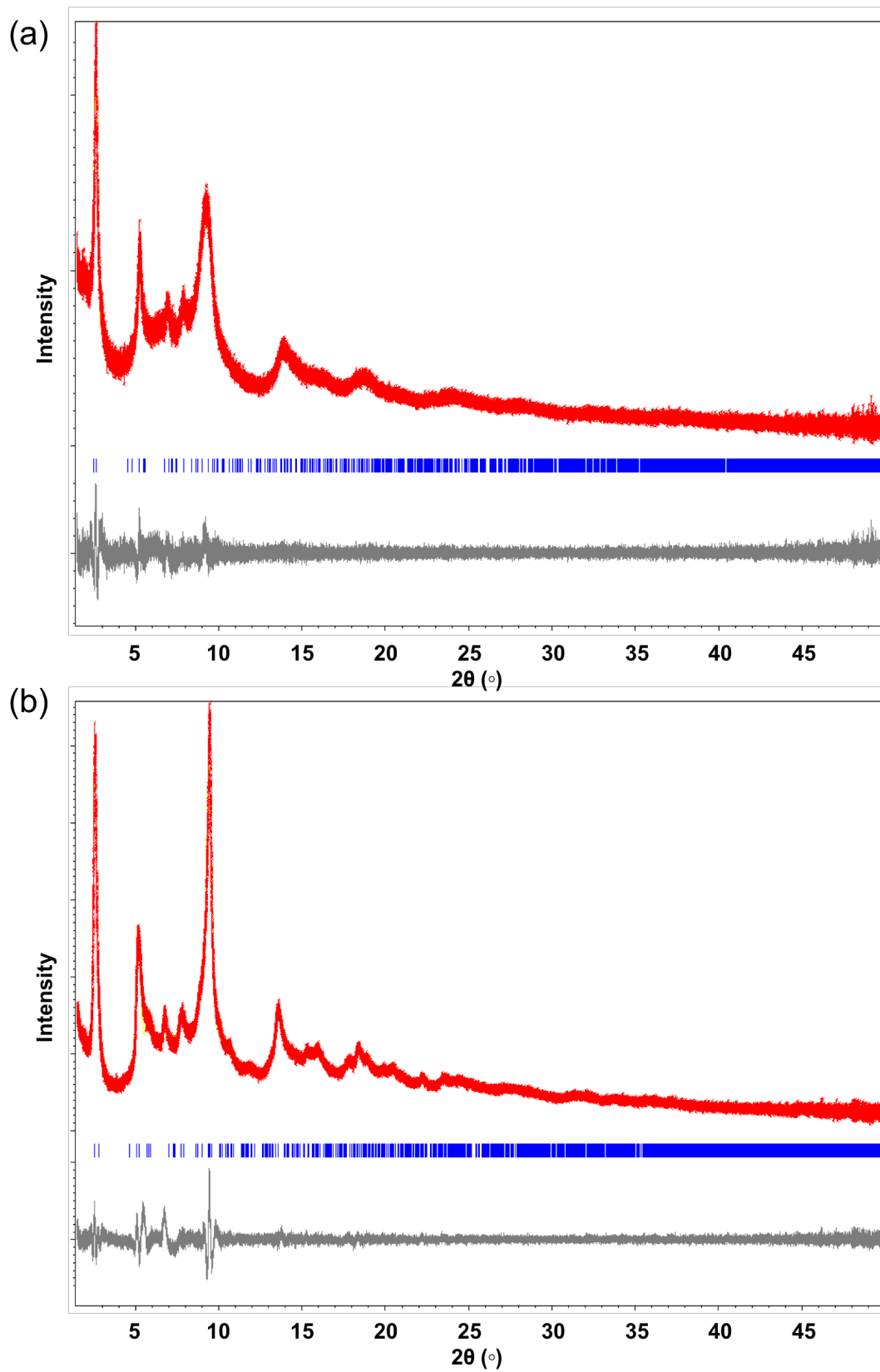


Figure S11. Le Bail refinement of the PXR D patterns of the two materials gave best fits for space groups $Cmcm$ and $C222_1$ for (a) $Ni_3(HIB)_2$ and (b) $Cu_3(HIB)_2$.

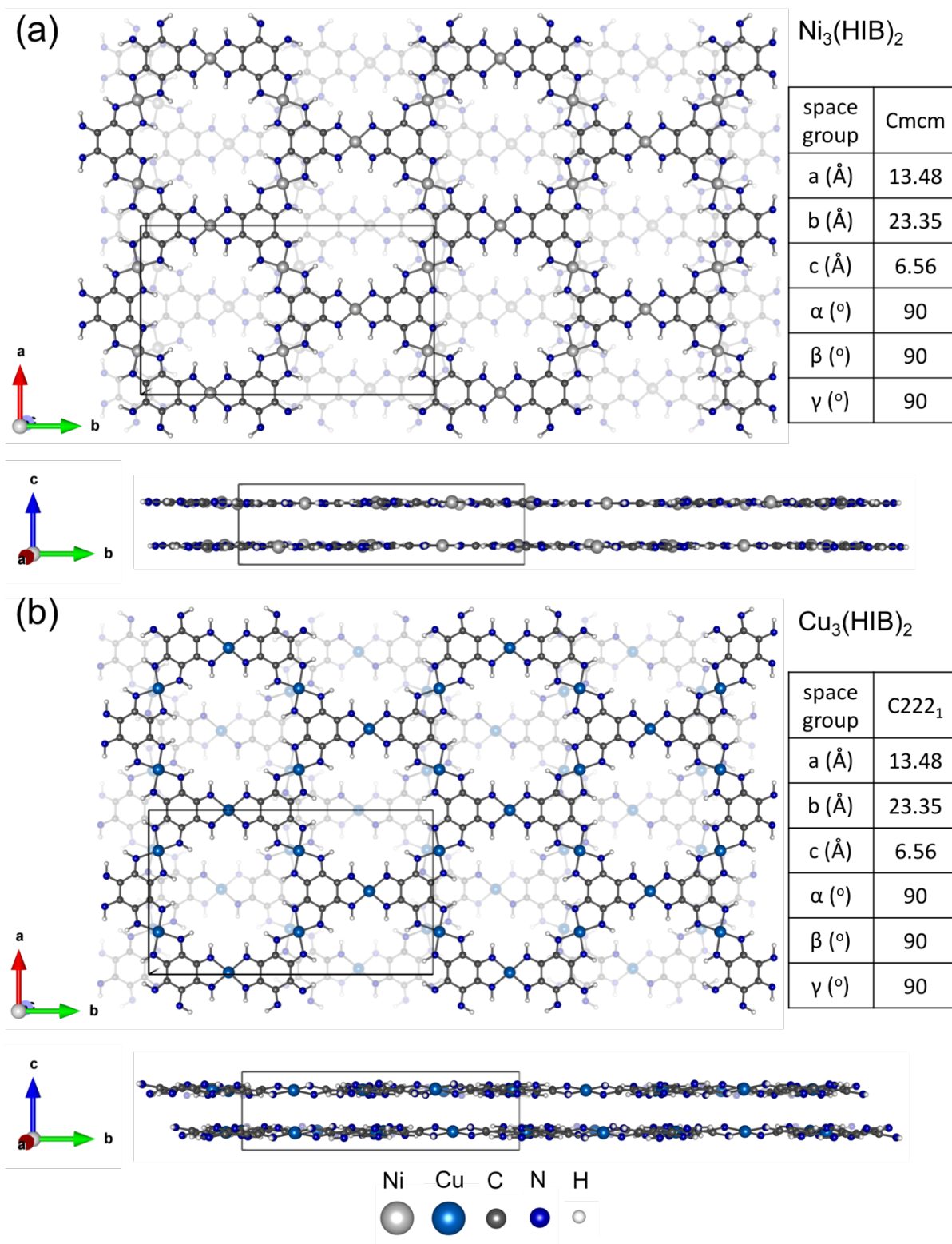


Figure S12. $\text{M}_3(\text{HIB})_2$ slipped-parallel structure with neighboring sheets displaced by (a) $0.24b$ for $\text{Ni}_3(\text{HIB})_2$ and (b) $0.27b$ for $\text{Cu}_3(\text{HIB})_2$. The fractional coordinates are with respect to the AA stacking in the b direction (according to the experimental data).

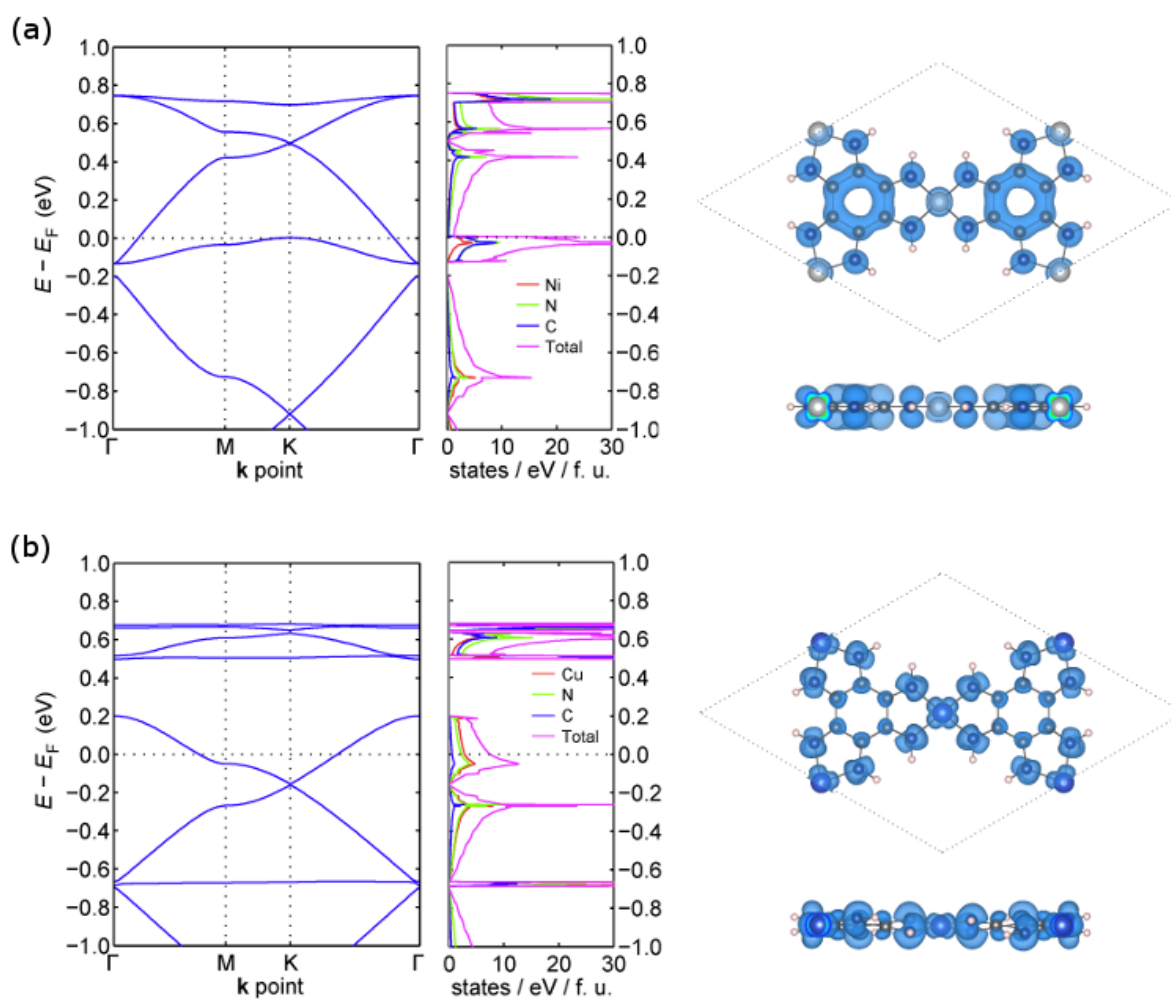


Figure S13. Calculated band structure, projected density of states, and charge density isosurface of electronic states near Fermi level ($E_F \pm 26$ meV) for *single layers* of (a) $\text{Ni}_3(\text{HIB})_2$ and (b) $\text{Cu}_3(\text{HIB})_2$. The DFT calculations were carried out using PBE exchange-correlation functional.

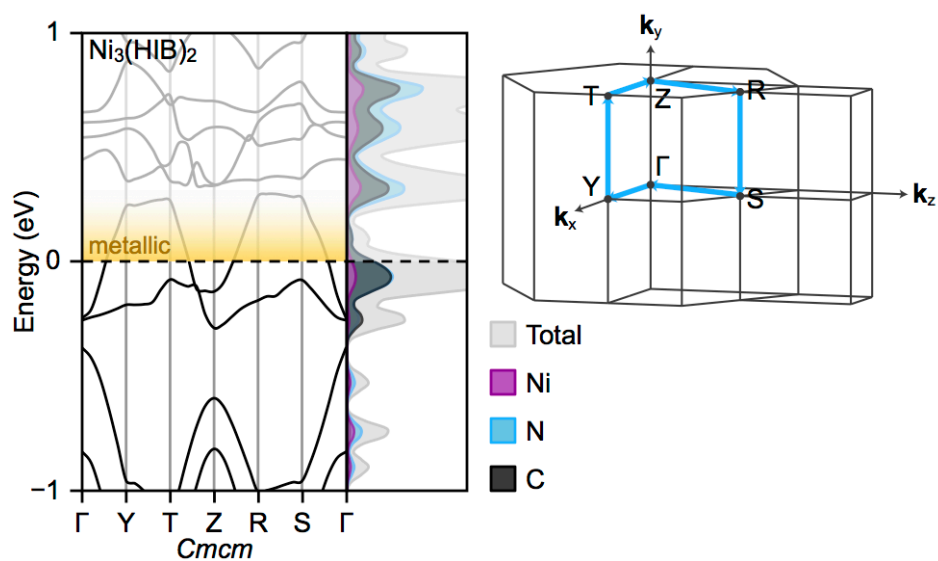


Figure S14. The representative $\text{Ni}_3(\text{HIB})_2$ bulk band structure, calculated using the HSE06 functional (as implemented with 25% HF exchange). The path in reciprocal space is shown schematically on the first Brillouin zone. $\text{Ni}_3(\text{HIB})_2$ is metallic as evidenced by non-zero density at the Fermi level.

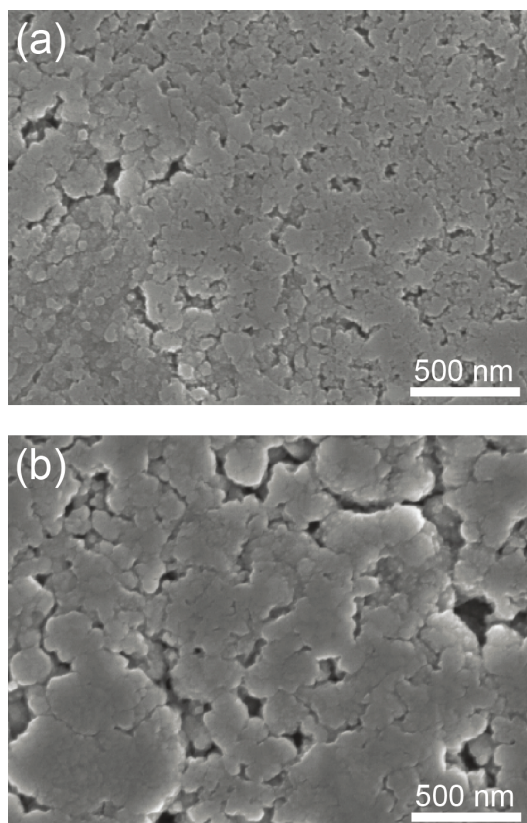


Figure S15. SEM micrographs for pressed pellets of (a) $\text{Ni}_3(\text{HIB})_2$, (b) $\text{Cu}_3(\text{HIB})_2$.

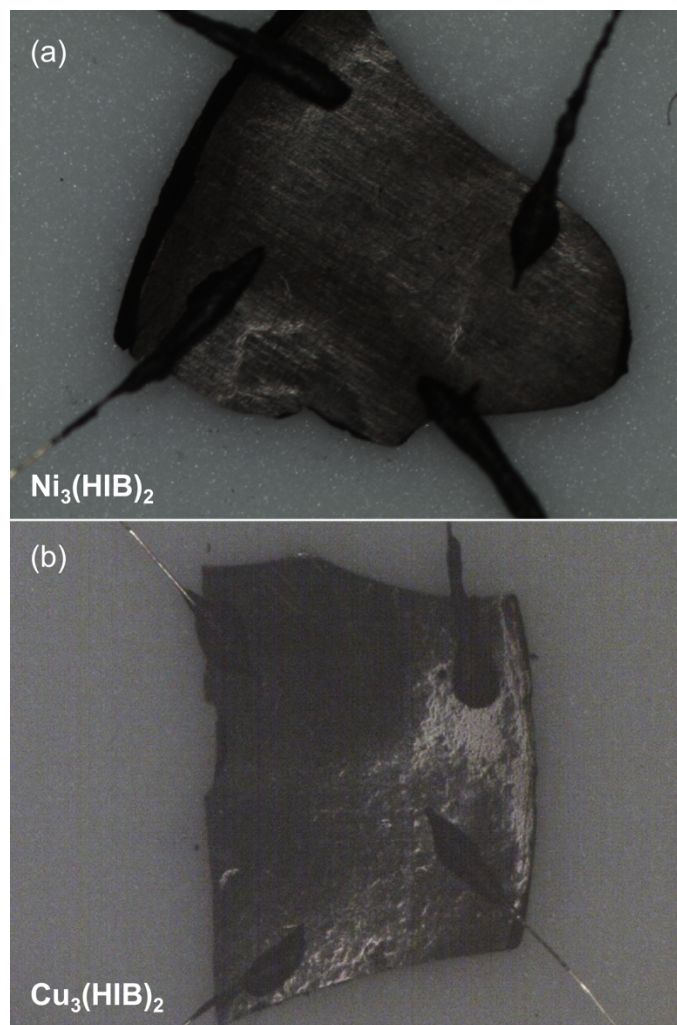


Figure S16. Pressed pellet devices used for the electrical conductivity measurements of (a) $\text{Ni}_3(\text{HIB})_2$ and (b) $\text{Cu}_3(\text{HIB})_2$ by van der Pauw method.

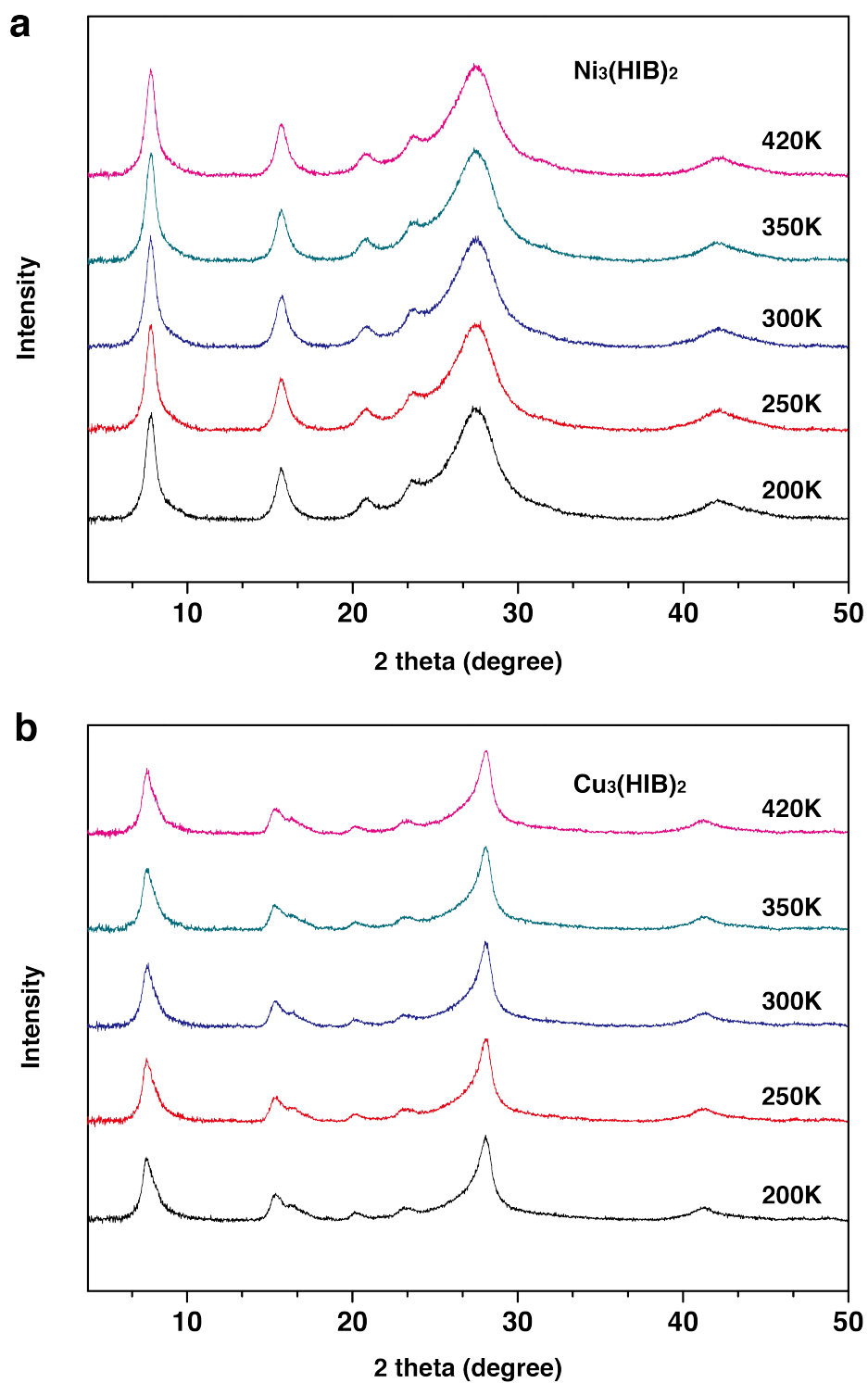


Figure S17. *In situ* PXRD patterns of $\text{Ni}_3(\text{HIB})_2$ and $\text{Cu}_3(\text{HIB})_2$ samples at 200 K, 250K, 300K, 350K and 420 K, using a wavelength of 1.5405 Å.

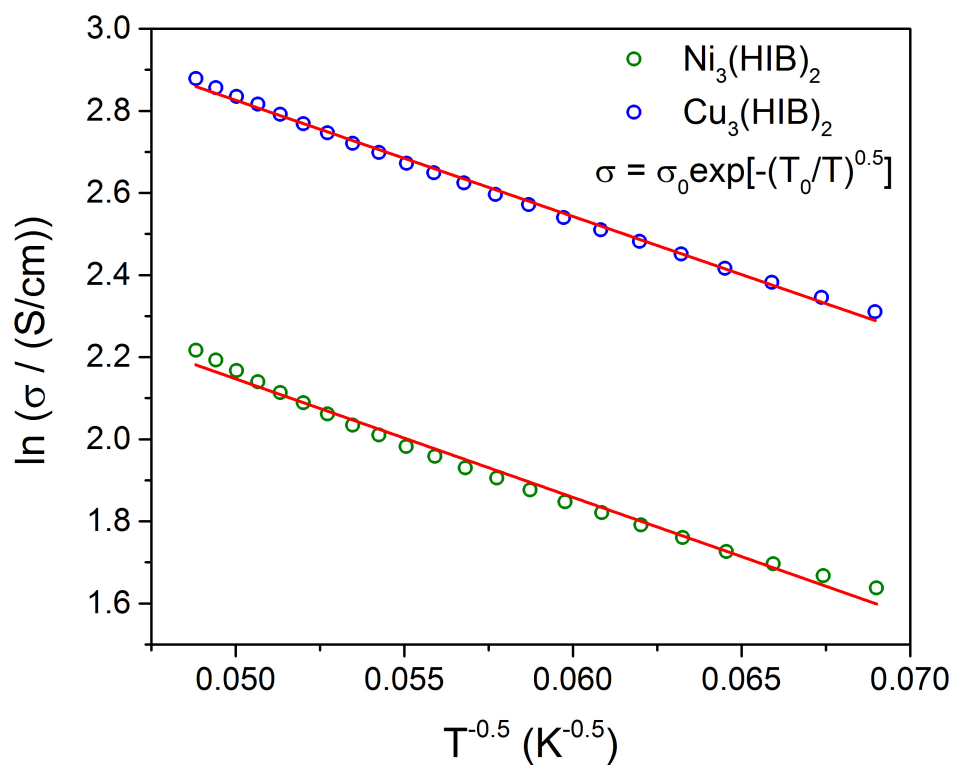


Figure S18. Granular metal model fitting of the conductivity of pressed pellets $\text{M}_3(\text{HIB})_2$ as a function of inverse \sqrt{T} , showing linearity between 200–420 K. $\sigma = \sigma_0 \exp[-(T - T_0)^{0.5}]$ where σ is electrical conductivity, T is absolute temperature, and σ_0 and T_0 are constants.

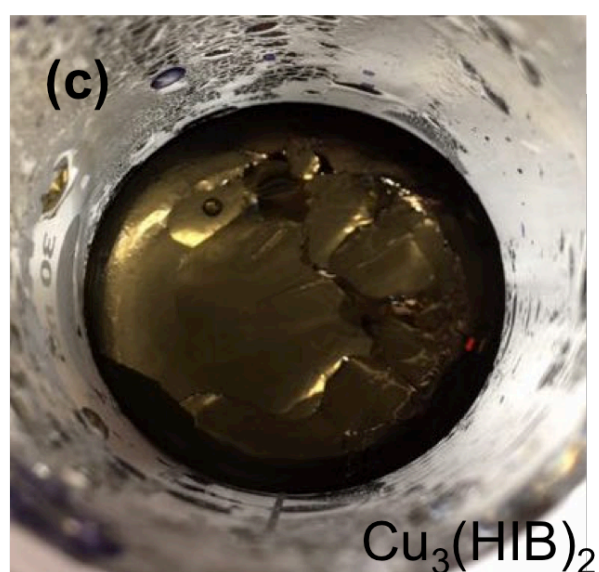
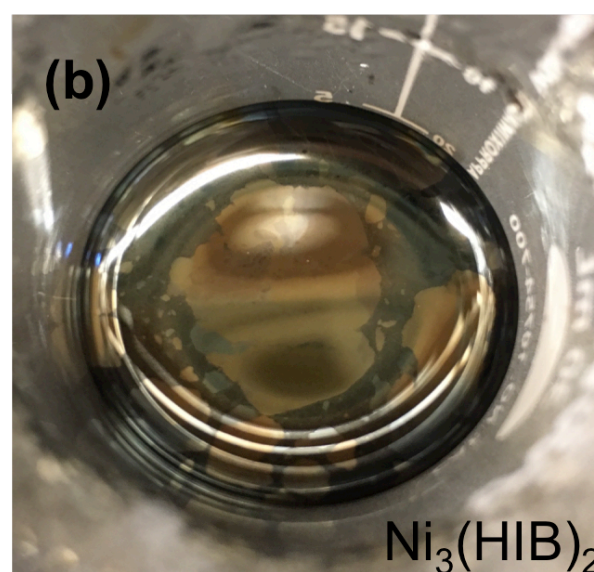
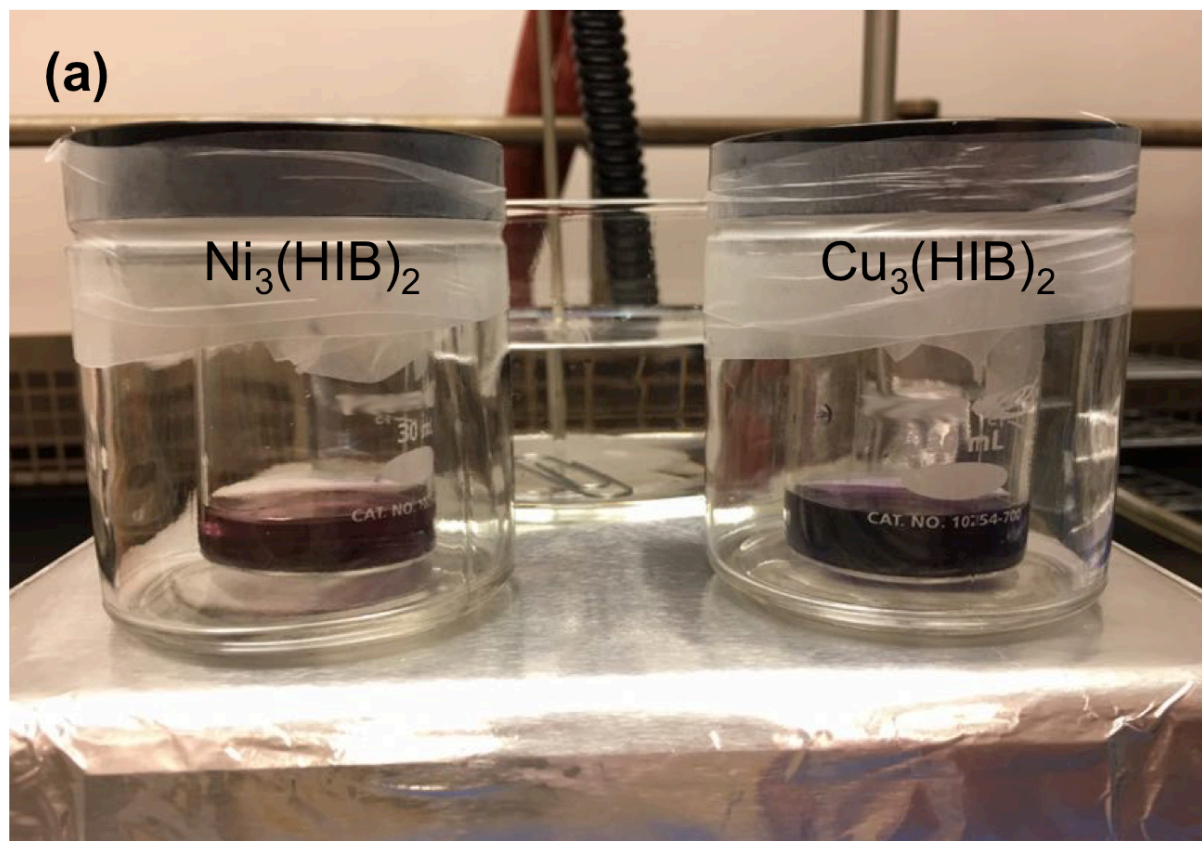


Figure S19. (a) The synthesis setup for $\text{Ni}_3(\text{HIB})_2$ (left) and $\text{Cu}_3(\text{HIB})_2$ (right). (b) $\text{Ni}_3(\text{HIB})_2$ film formed at the surface of the reaction mixture. (c) $\text{Cu}_3(\text{HIB})_2$ film formed at the surface of the reaction mixture. (Glassware branding has been digitally obscured upon request of the editor)

The degassed water allows slow introduction of oxygen onto the surface, thus enabling much slower growth of the MOF film compared to fully aerobic conditions. In addition, unlike organic solvents such as DMSO, water provides a platform where the hydrophobic MOF nanoparticles can gather at the gas-liquid interface to form a uniform layer due to the interface-confining effect. The reaction was further slowed down to improve the film quality by using ethylenediamine as the base due to its bidentately coordinating nature, which allows it to compete with HAB in binding the metal. The formation of the MOF thin film manifested as a dark thin layer with metallic shine at the gas-liquid interface.

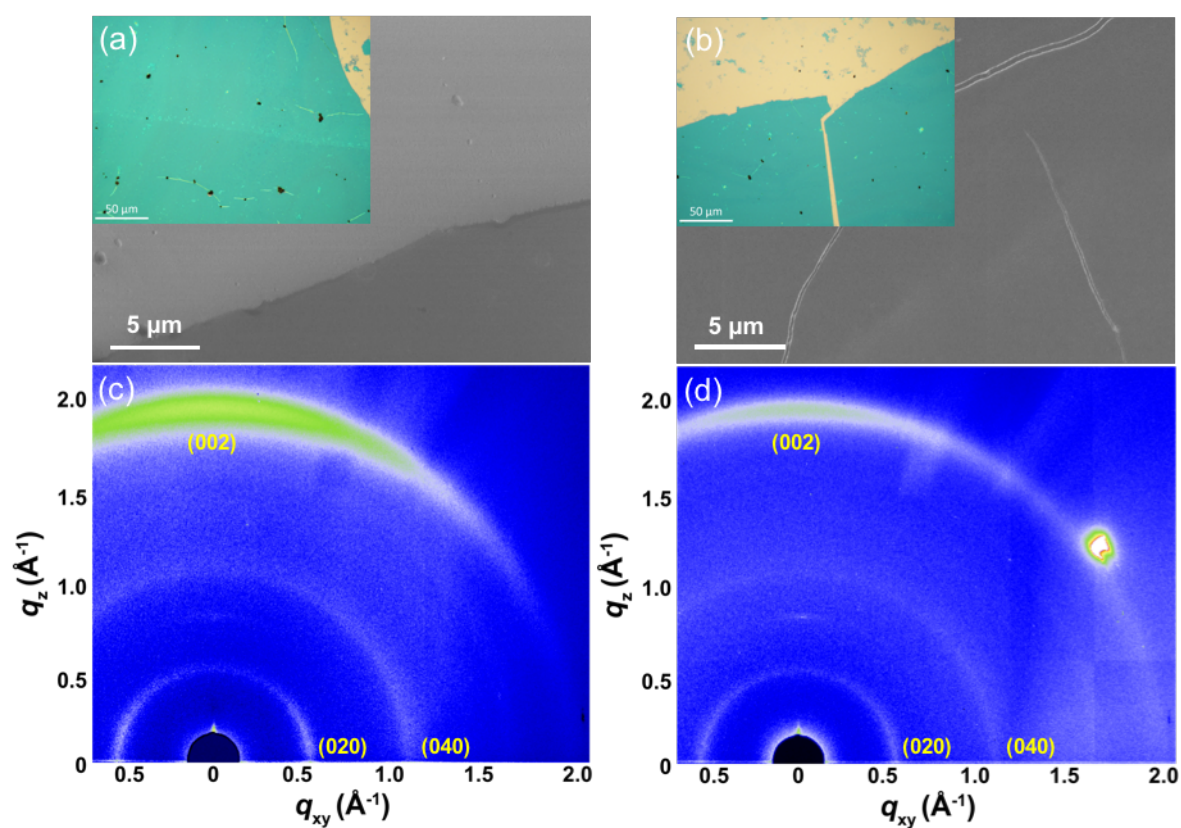


Figure S20. (a,b) SEM (inset optical micrograph) images of Ni₃(HIB)₂ and Cu₃(HIB)₂ top surface of film, respectively. (c,d) 2D-GIWAXS patterns of Ni₃(HIB)₂ and Cu₃(HIB)₂ films, respectively, fabricated under identical conditions.

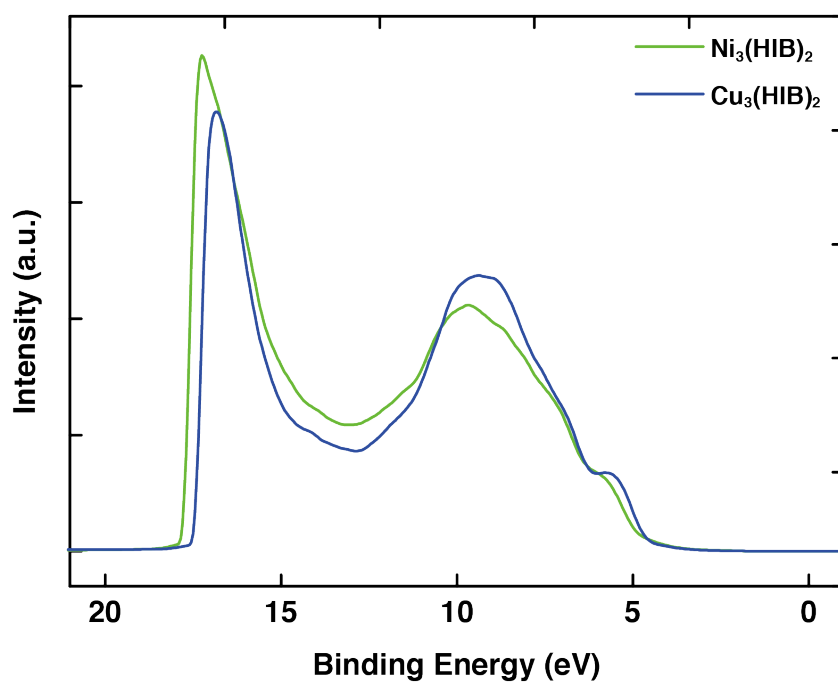


Figure S21. UPS of $\text{M}_3(\text{HIB})_2$ films acquired at 300 K.

6. References

1. Ravel, B.; Newville, M. *J. Synchrotron Radiat.* **2005**, *12*, 537.
2. Zabinsky, S.; Rehr, J.; Ankudinov, A.; Albers, R.; Eller, M. *Phys. Rev. B* **1995**, *52*, 2995.
3. Sun, L.; Park, S. S.; Sheberla, D.; Dincă, M. *J. Am. Chem. Soc.* **2016**, *138*, 14772.
4. Mahmood, J.; Kim, D.; Jeon, I.-Y.; Lah, M. S.; Baek, J.-B. *Synlett.* **2013**, *24*, 246.